



Article

Biotic–Abiotic Influences on Modern Ca–Si-Rich Hydrothermal Spring Mounds of the Pastos Grandes Volcanic Caldera (Bolivia)

Cédric Bougeault ^{1,*}, Emmanuelle Vennin ¹, Christophe Durlot ¹, Elodie Muller ²,
Mathilde Mercuzot ¹, Marco Chavez ³, Emmanuelle Gérard ², Magali Ader ²,
Aurélien Virgone ⁴ and Eric C. Gaucher ⁴

¹ Biogéosciences, UMR 6282 CNRS, Université Bourgogne Franche-Comté, 6 boulevard Gabriel, 21000 Dijon, France; emmanuelle.vennin@u-bourgogne.fr (E.V.); christophe.durlot@u-bourgogne.fr (C.D.); mathilde.mercuzot@univ-rennes1.fr (M.M.)

² Université Paris, Institut de Physique du Globe de Paris, UMR 7154 CNRS, F-75005 Paris, France; emuller@ipgp.fr (E.M.); emgerard@ipgp.fr (E.G.); ader@ipgp.fr (M.A.)

³ TOTAL E&P, 40 Calle Las Violetas, Edificio Arcus, Santa Cruz de la Sierra, Bolivia; marco.chavez@total.com

⁴ TOTAL CSTJF, Avenue Larribau, 64018 Pau Cedex, France; aurelien.virgone@total.com (A.V.); eric.gaucher@total.com (E.C.G.)

* Correspondence: cedric.bougeault@u-bourgogne.fr; Tel.: +33-380396371

Received: 29 April 2019; Accepted: 21 June 2019; Published: 23 June 2019



Abstract: The lacustrine-to-palustrine Pastos Grandes Laguna (Bolivia) is located in a volcanic caldera fed by active hot springs, with a carbonate crust extending over 40 km². An integrated approach based on geology and hydrochemistry was used to characterize La Salsa, one of its hydrothermal systems, composed of a flat mound with a hydrothermal discharge. The mound is composed of carbonate–diatom aggregates, forming muds that accumulate and undergo slight swelling. The discharge area along the hydrothermal pathway exhibits several facies and microfabrics, with considerable biological activity and microbialite development. Both the downstream evolution of carbonate and silica content in sediments and the distribution of microbialites can be linked to changes in biotic–abiotic processes occurring along the pathway. The spatial distribution of microbialites and their morphologies are related to hydrodynamic conditions, the nature of the substrate on which they grow and, to a lesser extent, to the accommodation space available. The evolution of the physicochemical properties of the water and biological activity mainly impact mineral precipitation but also affect microbialite morphologies and microstructures. This atypical Si- and Ca-rich hydrothermal system therefore provides insights into the diversity of environmental, chemical, and biotic factors controlling mineralization, which also responds to independent thermodynamic controls.

Keywords: Pastos Grandes Laguna; volcanic context; continental deposits; hydrothermal spring; flat mound; microbialites; mixed carbonate–silicate precipitation

1. Introduction

Hot springs are commonly associated with both active and dormant volcanic regions, as magmatic fields continuously release heat in different tectonic settings, including subduction [1–4] rifting [5,6], and intraplate volcanism [7,8]. They are fed with water enriched in ions acquired from the surrounding bedrock during fluid migration to the surface. High concentration in ions can lead to oversaturation, thus favoring mineral precipitation. In hydrothermal continental settings, the dissolution of nearby carbonate rocks and the decrease in CO₂ resulting from degassing or microbial activity at the surface lead to the formation of travertines [7,9,10]. In purely volcanic environments with no carbonate

rocks in the catchment area, the alteration of igneous rocks often leads to the formation of siliceous sinters [2,5,11–13]. Silica precipitation is mainly driven by temperature changes (evaporation or water cooling) [1,2,14,15], while microbial activity acts as a support for silica nucleation [12,13,16,17]. On rare occasions, in volcanic settings, whether Modern [6,18–21] or in the fossil record [22], hydrothermal travertines and mixed carbonate–silicate deposits may be observed. Such deposits may provide insights into the formation of South Atlantic Pre-Salt deposits [23,24].

At the southern part of the Bolivian Altiplano, the Pastos Grandes Laguna (120 km²) is a complex lacustrine-to-palustrine system of Recent to Modern deposits, including carbonates, evaporites, and Si-rich sediments. Numerous giant pisolites (up to 20 cm in diameter) can be observed [25], with a cortex composed of alternating layers of micritic or sparitic calcite and amorphous silica [26]. These pisolites are formed by abiotic processes promoting mineral oversaturation [25,26], while the presence of microbial mats and diatoms [26,27] may also play a role in mineralization [28]. Pisolite accumulations occur in shallow pools at the surface of a palustrine carbonate crust (40 km²), a unique case in the Bolivian Altiplano, with active hydrothermal springs containing both Ca-rich and Si-rich sediments. These hydrothermal springs have been described as hillocks of black sandy ferri-ferrous material feeding the pisolite pools [25]. It has recently been shown that they are continuously fed by hot waters enriched in mantle-derived CO₂, with Ca and Si ions from the alteration of underlying igneous rocks [29,30].

In this study, the largely undocumented Pastos Grandes facies will be analyzed, together with microbial structure and water chemistry along the proximal–distal hydrological pathway feeding La Salsa, one of the major hot springs in the Pastos Grandes Laguna. The main aims are to investigate: (i) the processes leading to mound formation associated with spring-fed waters, (ii) the parameters controlling facies distribution and microbialite fabrics along the hydrothermal pathway, and (iii) the respective roles of biotic versus abiotic factors in mineralization. The main results provide keys for the interpretation of ancient sediments rich in Ca and Si, developing under volcanic influence.

2. Settings

2.1. Geological Setting

The Andean cordillera—resulting from the subduction of the Nazca oceanic plate beneath the South American continental plate—hosts the highest plateau in the world, associated with a magmatic arc known as the Altiplano-Puna Plateau. This plateau is approximately 1800 km long, 350 to 400 km wide, at an average elevation of 4000 m (Figure 1A) [31]. The eastern side of the Altiplano-Puna Plateau, the Eastern Cordillera, is composed of Paleozoic to Cenozoic rocks, structured by several major thrusts [31,32]. On the western side, the plateau is bounded by Miocene to Recent stratovolcanoes organized in an active volcanic arc, the Western Cordillera [31–33]. The Altiplano and Puna regions are separated by a 70,000 km² volcanic complex, between 21°S and 24°S [34,35]. The Altiplano-Puna Volcanic Complex (active from 11 to 0.7 Ma) is composed of numerous calderas and stratovolcanoes [35,36], aligned NW–SE, indicating a major NW–SE tectonic compressional phase [33]. This complex is underpinned by a 500,000 km³ low-velocity zone, the Altiplano-Puna Magma Body, which fed the volcanic province [35,37,38]. The Pastos Grandes Caldera Complex (PGCC) in the Lipez region of Bolivia (Figure 1A), was formed by two consecutive ignimbrite eruptions, the Chuchulla Ignimbrite and the Pastos Grandes Ignimbrite. These high-K dacite ignimbrites are similar in composition, with plagioclase, quartz, biotite, sanidine, and amphibole (Figure 1B) [36,39,40]. Sanidine ages using the ⁴⁰Ar/³⁹Ar method give 5.45 ± 0.02 Ma for the first pulse, and 2.89 ± 0.01 Ma for the second [36]. A well-preserved caldera wall bounds the eastern flank, while the western flank is crosscut by several Pliocene dacitic stratovolcanoes [33]. Inside the caldera, several lakes and salars cover the ignimbrite deposits (Figure 1B).

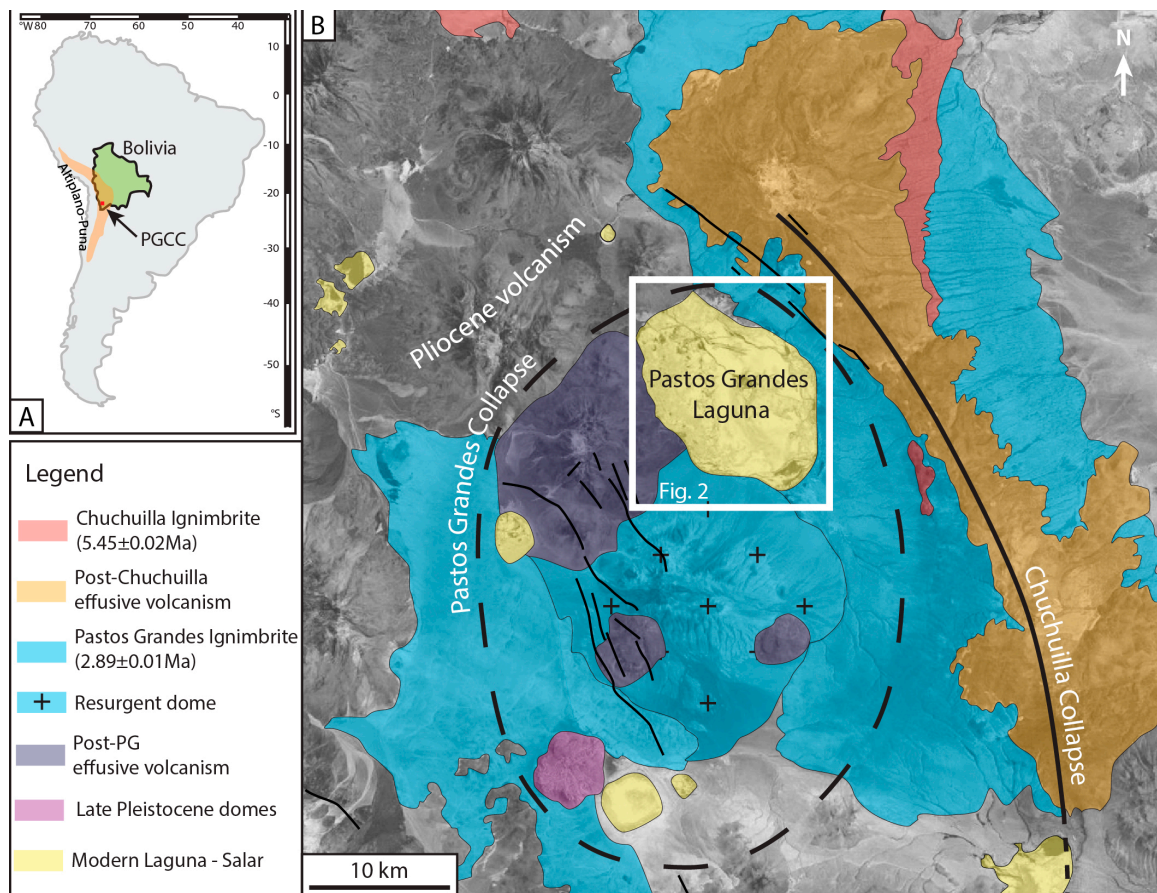


Figure 1. (A) General map of South America, showing the Pastos Grandes Caldera Complex (PGCC). (B) Satellite view of the PGCC, mapping associated volcanic deposits (modified from Kaiser et al. [40]; satellite image provided by Zoom Earth website, © 2018 Microsoft Corporation Earthstar Geographics SIO). Black lines correspond to faults identified by Tibaldi et al. [33].

2.2. Climate

The PGCC is characterized by a cold, dry climate [41]. Although no local meteorological data are available for the South Lipez region, day-to-day images from MODIS satellites show that most of the precipitation is summer rainfall, from December to March (EOSDIS Worldview, NASA), with an annual mean of 100 mm/yr [42,43]. During the rest of the year, dry conditions dominate, with a high evaporation rate of approximately 1400 mm/yr [27]. Air temperature can rise to +25 °C during the austral summer and drop to −30 °C in the austral winter [44]. The maximum daily temperature range can be as high as 40 °C [44].

2.3. The Pastos Grandes Laguna

The Pastos Grandes Laguna (−21.64 N; −67.79 E) is the largest salar in the PGCC. It culminates at 4440 m and covers approximately 120 km², with an elliptical shape oriented NNW–SSE. Its lacustrine-to-palustrine deposits have been classified as a playa [45]. The lacustrine area is completely submerged during the wet season, whereas the palustrine area is only partially covered by smaller pools (Figure 2B). The basin catchment is approximately 700 km², with the Chuchulla scarp to the east, a resurgent dacitic dome, formed after the caldera collapse, to the south, and Pliocene stratovolcanoes to the north (Figure 1B) [33,36,39,40]. The eastern side of the Pastos Grandes Laguna is fed by cool, ephemeral freshwater streams flowing from the Chuchulla scarp (see Table S1 and Figure 2A) [25]. The western and northern parts are fed by Piedmont springs, with either warm saline water, or cool fresh water (see Table S1 and Figure 2A). During the wet season, these springs feed a

large, shallow central lake, up to 60 km² (Figure 2B). During the dry season, the springs gradually dry up, sometimes causing total evaporation of the central lake (Figure 2C).

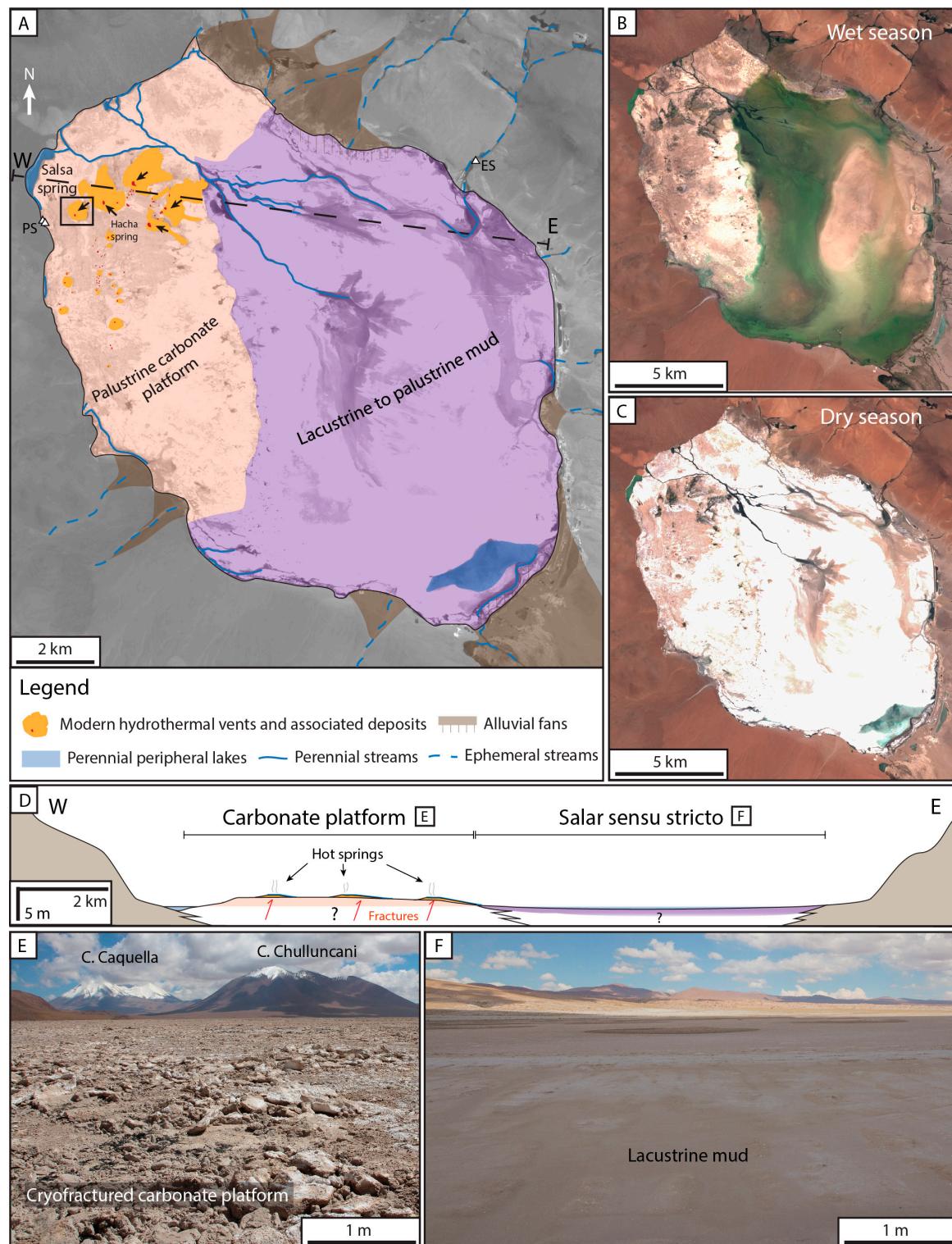


Figure 2. (A) Distribution of the main sedimentary environments of the Pastos Grandes Laguna (background map: Copernicus Sentinel Hub, Sentinel-2 image, October 6, 2017). Black arrows indicate Hacha, Salsa, and three other unnamed major hot springs. Triangles indicate water chemistry measurements on an ephemeral stream (ES) and two Piedmont springs (PS). (B) Satellite view of the

Pastos Grandes Laguna during the wet season (Copernicus Sentinel Data (2019), Sentinel-2 image, February 18, 2019). (C) Satellite view of the Pastos Grandes Laguna during the dry season (Copernicus Sentinel Data (2019), Sentinel-2 image, 6 October 2017). (D) Schematic east–west cross-section of the Pastos Grandes Laguna (see Figure 2A) showing the main hydrothermal springs. (E) Overview of the carbonate platform, disrupted by cryofracturation and cryoturbation, on the western side of the Pastos Grandes Laguna, with two volcanoes, Cerro Caquella (5950 m) and Cerro Chulluncani (5490 m), in the background. (F) Overview of the flat muddy salar (mainly comprising gypsum, volcanic detrital grains, micrite, and diatoms) in the eastern part of the Pastos Grandes Laguna, where ulexite is exploited in places.

The Pastos Grandes Laguna sediments were first described by Ahlfeld [46], and later by Ballivian and Risacher [45]. The eastern part of the salar exhibits a wide playa-lake palustrine environment, with mud containing gypsum and clay (Figure 2A,D,F). Mud may contain diatoms, volcanic rock particles, and Mg-rich clay minerals (stevensite) [27,47,48]. The central lacustrine area is also composed of gypsiferous mud associated with ulexite, a borate mineral ($\text{NaCaB}_5\text{O}_9 \cdot 8\text{H}_2\text{O}$) commonly extracted for borate production [49,50].

The western part is characterized by a carbonate-rich palustrine platform (hereafter, carbonate platform) covering approximately 40 km² (Figure 2A,D,E). It consists of a 20–30 cm-thick calcitic and siliceous crust, fragmented into decimeter- to meter-sized slabs, probably because of cryoturbation in this high-altitude context (Figure 2E) [25]. The platform is mainly composed of ooids, pisolites, bushy structures, and micritic accumulations [25,26]. The calcitic crust is approximately one meter above the average level of the central lake, and probably formed during the Late Pleistocene or Early Quaternary, when lake levels in the Bolivian Altiplano were generally higher [51–54]. Currently, Modern carbonate and silicate minerals precipitate where waters temporarily or permanently occupy areas of the palustrine platform. The most spectacular Modern carbonate deposits are giant pisolites, reaching up to 20 cm in diameter [25,26]. An age of 620 ± 220 yr B.P. has been determined for one of these pisolites [55].

The northern part of the platform is also characterized by five major hot spring systems, close to each other but not aligned, possibly resulting from underlying fractures, currently masked by the Recent carbonate platform (Figure 2A). Each hot spring forms a central pool (200 to 13,000 m²), located on a flat mound less than 2 m high, but which may exceed 500,000 m² in surface area. Figure 3A shows the Salsa spring, with bubble plumes at the surface indicating hydrothermal vents. Steam plumes from the hot springs are sometimes visible from the shoreline when the air temperature is low (Figure 3B). The Hacha spring (Figure 3C) contains a reddish central “chimney”, probably rich in iron oxides, but not examined during field investigations. Hydrothermal waters from these springs are enriched in numerous chemical elements, resulting from fluid–rock interactions during deep fluid circulation within volcanic rocks, and mantle-derived CO₂ [29,30]. Beyond the central pools, thermal waters flow through one or more shallow channels along the flanks of the flat mounds, before seeping through the fragmented carbonate crust of the platform.

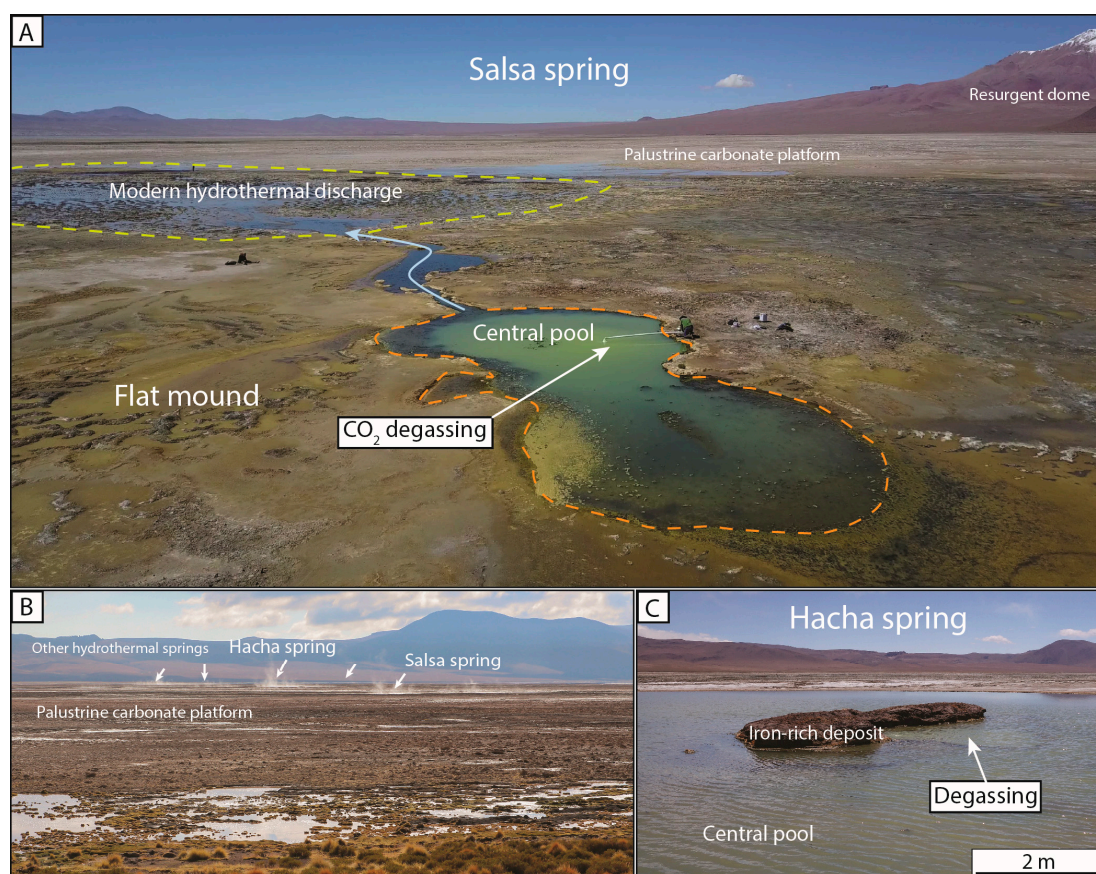


Figure 3. Examples of major hot springs in the northern part of the Pastos Grandes palustrine carbonate platform (see Figure 2A for location). (A) Air-drone view of the central pool (28 m long) of the “Salsa” hydrothermal system and its outflow. (B) Wisps of steam from major active hot springs. (C) Central pool of the “Hacha” hot spring, showing a dissymmetric iron-rich chimney at the center of the pool, close to the active vent.

3. Materials and Methods

Field investigations at the Pastos Grandes Laguna were carried out in January 2016 and March 2017. January 2016 was marked by a dry episode, with much less precipitation than in March 2017. All sediments described in the present study were collected around the hydrothermal La Salsa spring, less than one kilometer from the shoreline, on the northwestern part of the carbonate platform (−21.6193 N; −67.8484 E; see Figure 2A). The 22 samples of sedimentary rock were collected along a single stream flowing from La Salsa, the central hydrothermal vent. Facies were mapped by attributing GPS coordinates to samples, which were then spatially aligned on a mosaic of aerial images taken in March 2017 at 80 m above ground level, using a DJI Mavic Pro air drone. Several generations of Sentinel-2 satellite images (Copernicus Sentinel data, 2019), together with images from Google Earth Pro software, were used to contextualize La Salsa at the scale of the entire carbonate platform and the Pastos Grandes Laguna.

During field investigations, in situ physicochemical measurements of hydrothermal waters were acquired using a Hach HQ40D Multi instrument, with temperature (*T*), pH, conductivity (*EC*), and O₂ concentration (%) sensors. Specifically for the samples from January 2016, (1) water alkalinity was measured in the field, using 1 μm filtered water, by titration with sulfuric acid and (2) water chemical composition was analyzed at the BRGM (French Geological Survey, Orléans, France) and Total (Pau, France) laboratories, using ion chromatography, atomic absorption spectrophotometry, inductively coupled plasma mass spectrometry (ICP-MS), colorimetry, the ion electrode method, and titration.

Facies observations were carried out at different scales on polished slabs and polished thin sections. Petrographic thin sections were observed under plane-polarized light (PPL) and cross-polarized light (XPL) using a Nikon AZ100 microscope (Nikon Corporation, Tokyo, Japan) coupled with a Zeiss MrC5 camera. Muddy sediments and rock shards were observed with a TM-1000 Hitachi SEM (Hitachi, Tokyo, Japan), for details of microbial and crystal morphologies. Thin sections were partially stained with alizarin Red-S and potassium ferricyanide (AF) to identify calcite and ferrous carbonates.

The biotic-rich facies were determined at macroscale, mesoscale, and microscale, following Shapiro [56]. Macroscale describes the general morphology of the biotic facies. Mesoscale (observable with the naked eye) focuses on the internal organization of the morphologies identified. Microscale focuses on the petrographic description of the components observed by microscope and SEM. Macroscopic structures may be microbialites, formed through the mineralization of benthic microbial mats and/or the trapping and binding of sedimentary particles [57].

Mineralogical components were analyzed using X-Ray Diffraction (XRD) at the Biogéosciences Laboratory (University of Burgundy, Dijon, France). Sample rocks were crushed and flattened without orienting crystals. Powders were analyzed using a Bruker D4 Endeavour diffractometer (Bruker, Billerica, MA, USA) with $\text{CuK}\alpha$ radiations, LynxEye detector, and Ni filter, under 40 kV voltage and 25 mA intensity. Scanning from the goniometer ranged from 2° to 65° for each analysis.

Calcium and silicon content of microbialites and muds was measured at the Biogéosciences Laboratory (University of Burgundy) with a XRF spectrometer (Bruker S1 TitanLE; Bruker, Billerica, MA, USA), to estimate the evolution of the Ca/Si elemental ratio along the pathway. Content was measured in whole rock and powdered samples, using two successive beam phases of 45 kV and 15 kV. Internal laboratory standards were used for empirical calibration of geochemistry, with a wide range of travertines and tufas documented in Teboul et al. [8]. Carbonate content was also independently measured using a Bernard calcimeter, by reacting carbonate with hydrochloric acid, to determine the volume of CO_2 released. Chemical mapping of polished slabs and thin sections used a micro-XRF technique, with a Bruker M4 Tornado spectrometer (Biogéosciences Laboratory, University of Burgundy), equipped with two SD detectors and a Cr anode X-ray tube (spot diameters of 25 μm).

Saturation indexes were computed using the geochemical code PHREEQC 3.0 (Version 3.0, USGS, Reston, VA, USA) along the hydrothermal pathway [58], with the BRGM “Thermoddem” database [59].

4. Results

The hydrothermal La Salsa spring is one of the five major springs observed in the Pastos Grandes Laguna. It is divided into two main spatial units, with seven facies, based on hydrology and sediment production: (1) La Salsa flat mound, with an ephemeral flow all around the central pool and (2) La Salsa main hydrothermal discharge, a perennial flow from the central pool along the eastern side of the flat mound. The hydrothermal spring lies on a carbonate platform composed of three main facies (Table 1): (1) laminated grainstone (F1a; Figure 4A); (2) massive grainstone (F1b; Figure 4B); and (3) pisolites (F1c; Figure 4C). The entire carbonate platform is affected by pedogenesis, as shown by in situ brecciation, dissolution, diagenetic grains [60,61], micritization, and blocky calcite cementation [62]. Grainstone composition is related to position on the carbonate platform, and laminated grainstones differ from massive grainstones only by their internal structure. Close to clastic feeding areas, grainstones are enriched in allochthonous components (detrital minerals from volcanic alteration: plagioclase, quartz, biotite, and amphibole) together with a relatively rich biotic content (i.e., bundles of microbial sheaths, gastropods, and ostracods). Micritic clasts and pisoids are often observed on the platform at some distance from springs and clastic inputs (ca. 100 m to 500 m). Micritic intraclasts, from several micrometers to several millimeters in diameter, are embedded in a calcitic spar-cement. Pisolites are concretions alternating between micritic laminae and radial bundles of sparry calcite, organized in concentric layers [25,26]. Amorphous silica layers are occasionally present in the carbonate-rich cortex. Pisolite nuclei usually consist of intraclasts of carbonate crusts, detrital grains, or calcitic spherulites.

Table 1. Facies characterization (composition, structure, and extension) and depositional environment.

Facies		Composition	Structure	Extension	Depositional Environment	Zone
F1: Facies of the carbonate platform	F1a: Laminated grainstone	Recent carbonate crust composed of detrital grains, intraclasts (micrite–sparite), ostracod valves, microbial filaments, and pisolites; Dominant components depend on the position on the carbonate platform, affected by cementation (sparite or micrite, locally iron hydroxide) and dissolutions	Porosity organized in laminae (birdeyes?) in F1a and scarce porosity in F1b; micritization of grains; circumgranular fractures; calcitic spar-cement infilling, local iron hydroxide cements	Up to 30 cm thick	Pedogenic (diagenetic grain and caliche formations) of lacustrine facies	Recent carbonate platform and locally observed in Zone IV
	F1b: Massive grainstone					
	F1c:Pisolites	Successive micritic and sparitic laminae developing around a nucleus (intraclast, spherulite, detrital grains)	Discoid to spherical pisolites	From few mm to 20 cm in diameter	Developed on carbonate platform	
F2: Mud to wacke sediments	F2a: Unconsolidated micritic mud	Orange to green layered mud, mainly aggregates composed of micrite, diatoms, cyanobacterial filaments, ostracod valves, and aragonite needles	Crudely layered	cm to dm thick	Domal mound facies	I
	F2b: Diatom mud	Reddish to black muds mainly composed of diatoms, micrite (and rare filaments)	Accumulation	mm to cm thick	Central pool	I
	F2c: Ostracod-rich mud	Brown to black mud composed of disarticulated ostracods, micrite, diatoms organized in aggregates, and rare filaments	Accumulation	Several hundred m ²	Along the slope from the channel to the proximal–distal transitional belt	II and III
F3: Amorphous deposits		Reddish crust composed of mineralized EPS in Si–Fe–Mg–As, affected by shrinkage cracks, with micritic intraclasts, coated by isopachous to pustular amorphous silica cements	Diagenetic structures	2–3 cm thick	Domal mound facies	Flat mound
F4: Pedogenic packstones–floatstones		Broken and corroded micritic intraclasts mixed with F2a, affected by circumgranular cracking, stained by Fe, porosity infilled by sparite cements and micrite	Clotted	cm to dm thick with intraclasts of 50 μm to 1 mm)	Reworked facies in pedogenized domal mound	I and II
F5: Microbial and diatomaceous bindstone	Ledge		Microbial laminae	Bordering edges	Central pool and channel	I
	Mushroom-like			Scarce	Channel	I
	Cerebroid			Scarce	Apron	II
F6: Diatomaceous and peloidal micropackstone		Snake-like	Microbial laminae	Covering more than 8000 m ²	Transitional proximal–distal belt	III
F7: Shrub		Isolated shrub, Planar shrub	Microbial laminae	Covering more than 46,000 m ²	Distal zone	IV IV

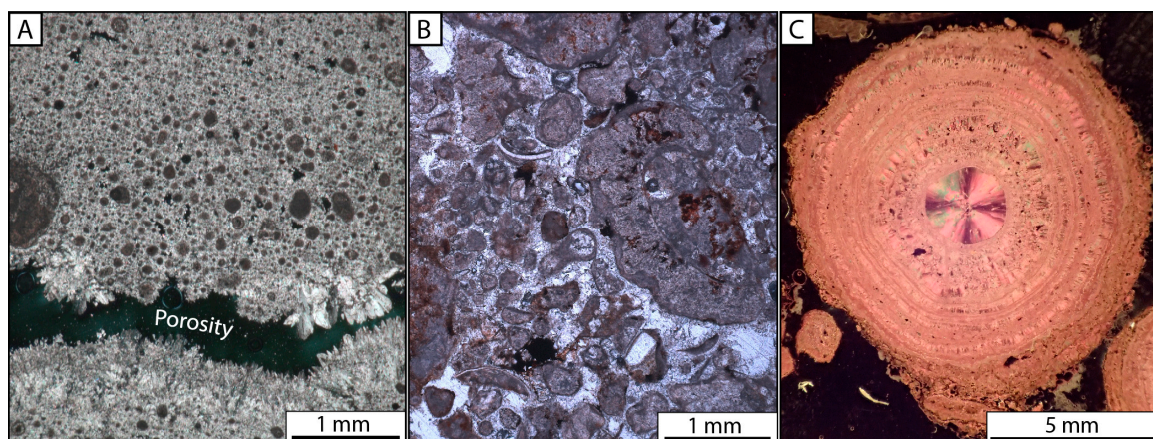


Figure 4. Three examples of facies from the Recent carbonate platform. (A) The cross-polarized light (XPL) view of a laminated grainstone, with small rounded micritic intraclasts, and sparse ooids cemented by a bladed to acicular calcite cement. (B) The plane-polarized light (PPL) view of a coarse grainstone, showing great grain diversity (micritic intraclasts, reworked microbialite fragments, detritic minerals, and ostracod shells), sometimes coated by Fe oxides or isopachous calcite cement. (C) The XPL view of a small pisolite (stained with AF), showing a nucleus formed of a calcitic spherulite, and a cortex of concentric sparite-micrite laminae (see Jones and Renaut [26]).

4.1. La Salsa Flat Mound

The subcircular flat mound, less than 1 m in height and approximately 300 m in diameter, curves slightly, with several overlapping rims at its edges (Figure 5A). The most distant rim lies directly on the carbonate platform (F1a-c). Numerous shallow dry channels characterized by muddy deposits and relicts from the carbonate platform (e.g., intraclasts) spread over the mound from the central pool.

An excavation pit (approximately 30 cm deep) was dug near the vent to provide access to the internal structure of the uppermost layers of the mound (Figures 5B and 6A). The top section (first 10 cm) is composed of rust-colored micritic aggregates and well-preserved diatoms, with black lenses rich in unconsolidated microbial filaments and diatomaceous sediments (F2a; Figure 6B). The next section (2–3 cm) is reddish ferrous crust, with intraclasts embedded in exopolymeric substance (EPS), containing Mg, Fe, and As. This EPS is affected by shrinkage cracks and coated by a silicate gel (F3, Figure 6C). The deepest section (20 cm) is greenish sediment composed of diatoms, calcitic aggregates, ostracod shells, and microbial filaments (F2a; Figure 6D). The position of the water table (the bottom 10 cm) is associated with a change in mineralization, marked by a dense network of aragonite needles covering the aggregates (Figure 6E).

Near the central pool and within the rims, some lithified sediments are identified as pedogenic packstones-floatstones (F4). Lithoclastic grains are dispersed within the unconsolidated diatom- and micrite-rich sediments (F2a). Some lithoclasts, composed of rounded micritic peloids (from a few hundred micrometers to a millimeter), organized in clusters and cemented by sparry calcite cements and affected by pedogenesis, correspond to reworked fragments of carbonate platform (Figure 6F). Other lithoclasts are identified as lithified mud facies (F2a) from the flat mound. Voids between these lithoclasts are partially filled by micritic internal sediment.

4.2. La Salsa Main Hydrothermal Discharge

Observations along the perennial hydrothermal drainage system at different scales (from satellite to microscope views) showed downstream zonation. Four main depositional zones (described in Section 4.2.3) were identified: (I) the hydrothermal feeding system, (II) the apron, (III) the proximal–distal transitional belt, and (IV) the distal zone. This zonation is based on water chemistry, the geometry of the water outflow, biosedimentary structures, biotic components, and mineralogy. The spatial distribution of these zones is presented on an idealized transect in Figure 7.

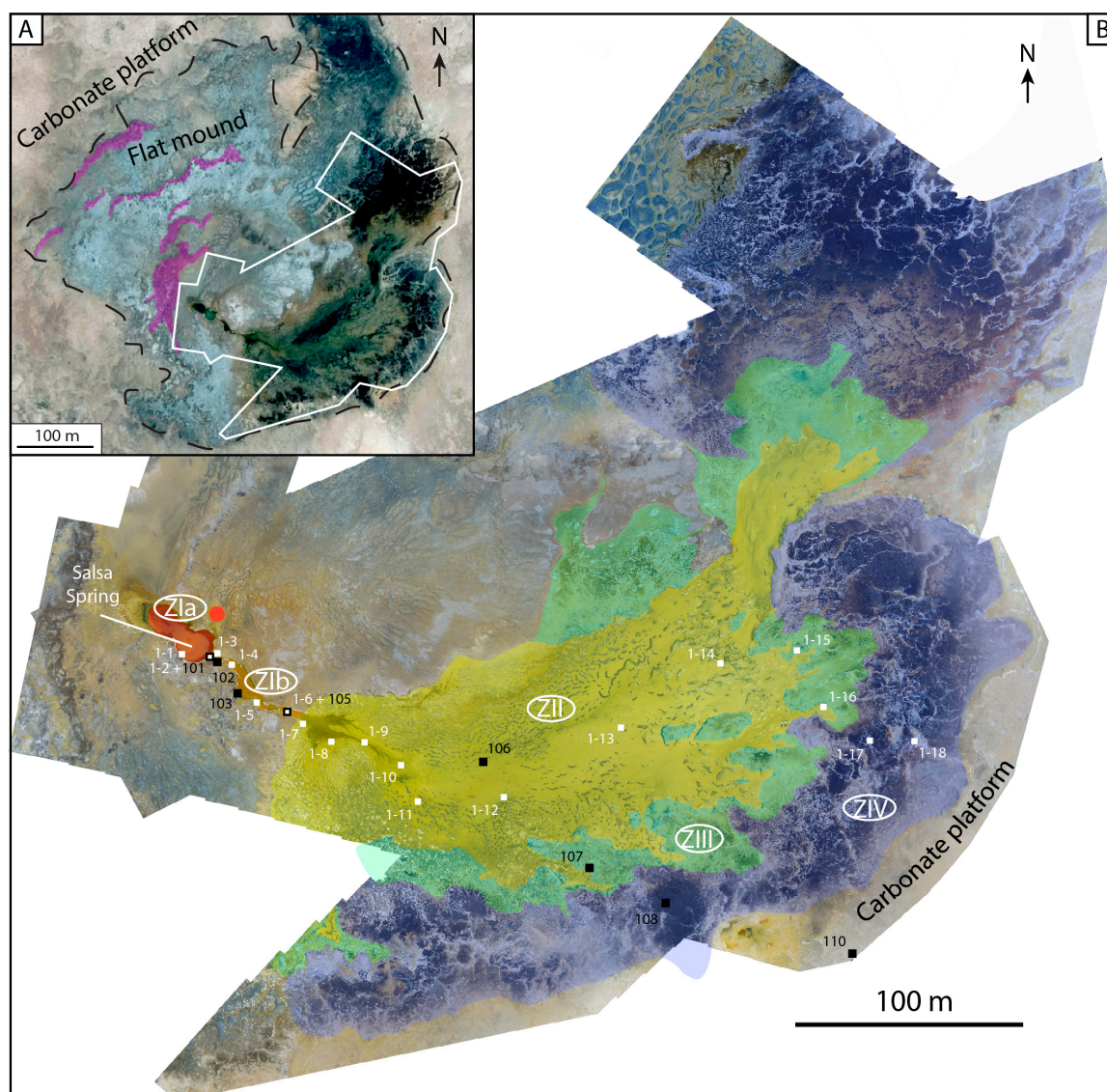


Figure 5. (A) Satellite view of the hydrothermal La Salsa system. The black dotted line separates the Modern hydrothermal system from the Recent carbonate platform. Purple areas correspond to examples of accretionary rims detected on the flat mound flanks (Image provided by Google Earth Pro Software © 2019 CNES/Airbus). (B) Air-drone stitched views of La Salsa, showing its main perennial depositional areas: Zone Ia—the central pool (in red); Zone Ib—the channel (in brown); Zone II—the apron (in yellow); Zone III—the proximal–distal transitional belt (in green); Zone IV—the distal zone (in blue). White dots indicate sampling from January 2016, and black dots from March 2017. The red dot corresponds to the excavation pit near the top of the flat mound (see Figure 6A).

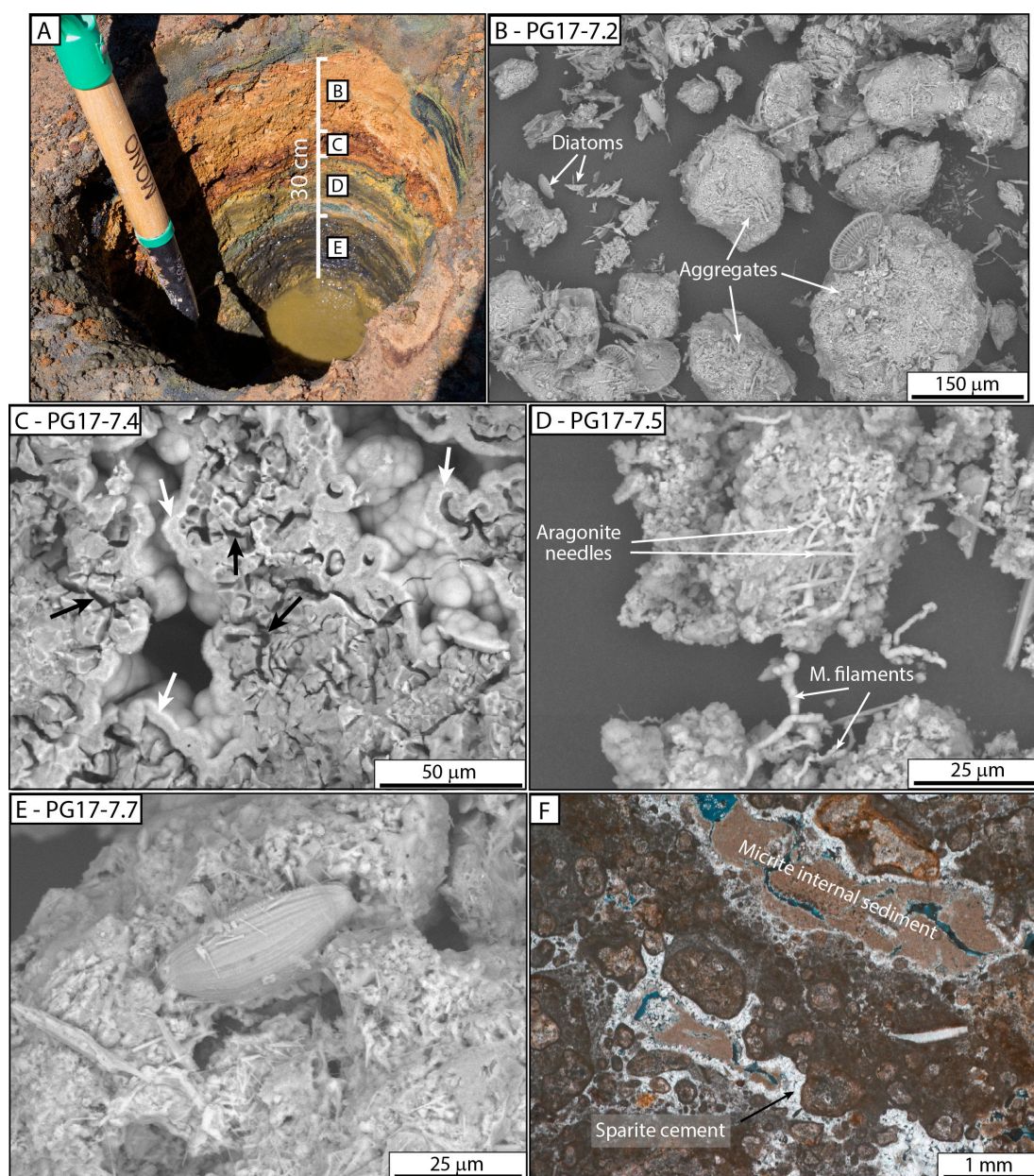


Figure 6. Main microfacies of the flat mound around La Salsa hot spring. (A) A 30-cm-deep excavation showing the laminated structure of La Salsa flat mound near the central pool (see Figure 5B for location). The rust color observed in the upper layer results from Fe oxides above the water table at the time of observation, whereas darker layers mainly develop near and below the water table. The greenish color of the intermediate layer is related to its richness in preserved microbial filaments. (B) The SEM view of the unconsolidated upper layer formed by small aggregates incorporating micritic crystals, diatom frustules, and microbial filaments. (C) The SEM view of the ferrous crust showing exopolymeric substance (EPS), rich in Si-Mg-Fe-As elements, and affected by shrinkage cracks (black arrows). The EPS constitutes a porous network, with pores coated by an isopachous to pustular cement of amorphous silica (white arrows). (D) The SEM view of soft sediment with aggregates of small anhedral crystals of calcite (micrite), microbial filaments, and diatom fragments. Aragonite needles develop around these aggregates. (E) The SEM view of an aggregate (diatoms and micrite) covered by a dense network of aragonite needles. (F) The PPL view of a pluricentimetric intraclast exposed on the flat mound flank. This reworked lithified sediment is formed by small intraclasts and micritic peloids, embedded in layers of dense to clotted micrite. Large voids between these layers were first cemented by sparry calcite, and then filled by brown micritic internal sediment.

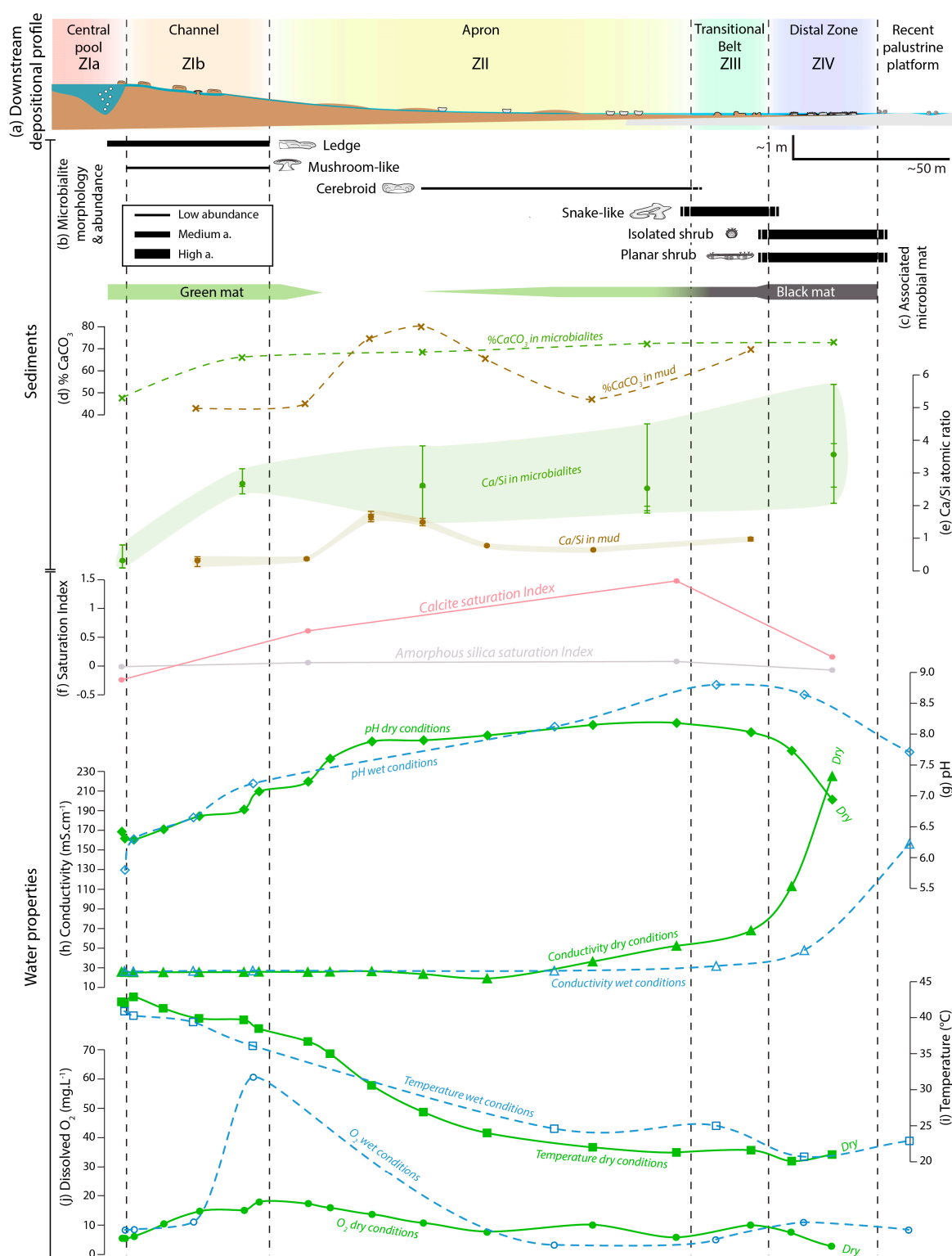


Figure 7. Downstream evolution of facies (microbialites and muds) shown in relation to their geochemistry and associated parent waters. **(a)** downstream depositional profile, showing sedimentary zones Ia to IV; **(b)** microbialite morphology and abundance; **(c)** distribution and color of microbial mats; **(d)** carbonate content (%) of microbialites and mud (Bernard calcimeter); **(e)** Ca/Si atomic ratio of microbialites and mud (bulk XRF measurements); **(f)** computed saturation index for calcite and amorphous silica (Thermoddem database, PHREEQC software); **(g)–(j)** physicochemical parameters from field measurements (January 2016 and March 2017), with dots indicating sampling sites: **(g)** pH, **(h)** conductivity, **(i)** temperature, **(j)** dissolved O_2 concentration.

4.2.1. Water Properties

Physicochemical parameters from hydrothermal waters, measured in January 2016 (dry episode) and in March 2017 (wet season), record major changes along the entire transect from the central pool to the distal zone (Figure 7g–i and Table 2). In the central pool (Zone Ia), the expelled water is slightly acid (pH= 6.35), with a temperature of approximately 42 °C, and moderate conductivity (26 mS·cm^{−1}). As it flows through the channel (Zone Ib), and spreads on to the apron (Zone II), the water becomes neutral to slightly alkaline, and the temperature drops from 36 to 20 °C. Values recorded in dry and wet conditions show no real change in these proximal zones. By contrast, pH and conductivity show strong variations between dry and wet conditions in the distal zones, although water temperature remains around 20 °C, as both fieldwork investigations took place during the winter season. In dry conditions, a stable pH of 8.2 is observed in the apron (Zone II), decreasing in the distal zone (Zone IV), where pH values can be lower than 7 in isolated ponds. Conductivity values remain stable in the middle of the apron (25 mS·cm^{−1}), and increase in the distal zone (225 mS·cm^{−1}). No results were obtained for the Recent carbonate platform, which is totally dry and covered by a saline crust. In wet conditions, pH increases progressively up to ca. 8.8 in the transitional belt (Zone III) before decreasing to pH of 8 in the distal zone (Zone IV). Conductivity is stable around 25 mS·cm^{−1}, and increases slightly in the distal zone up to 48 mS·cm^{−1}. However, a major increase up to 150 mS·cm^{−1} is observed on the Recent carbonate platform, when the flooded pools become interconnected with the hydrothermal La Salsa system.

Table 2. Physicochemical water measurements along the hydrothermal La Salsa pathway in January 2016 and March 2017.

Points	Zone	Latitude	Longitude	pH	Conductivity (mS·cm ^{−1})	Temperature (°C)	Oxygen (mg·L ^{−1})
Dry conditions (January 2016)							
PG1-1	Z-Ia	21.61934°S	67.84842°W	6.42	25.90	42.20	5.51
PG1-2	Z-Ia	21.61934°S	67.84836°W	6.31	25.80	42.00	5.50
PG1-3	Z-Ib	21.61934°S	67.84832°W	6.29	25.40	42.90	6.15
PG1-4	Z-Ib	21.61941°S	67.84825°W	6.46	25.50	41.30	10.42
PG1-5	Z-Ib	21.61950°S	67.84817°W	6.67	25.60	39.90	14.70
PG1-6	Z-Ib	21.61951°S	67.84805°W	6.78	25.70	39.70	15.00
PG1-7	Z-II	21.61955°S	67.84801°W	7.07	26.00	38.50	17.80
PG1-8	Z-II	21.61962°S	67.84782°W	7.23	25.80	36.70	17.30
PG1-9	Z-II	21.61960°S	67.84771°W	7.60	26.10	35.00	15.90
PG1-10	Z-II	21.61974°S	67.84759°W	7.88	26.50	30.60	13.60
PG1-11	Z-II	21.61987°S	67.84746°W	7.90	23.60	26.90	10.70
PG1-12	Z-II	21.61978°S	67.84722°W	7.98	19.28	24.00	7.60
PG1-13	Z-II	21.61955°S	67.84689°W	8.15	36.40	22.00	10.00
PG1-14	Z-II	21.61929°S	67.84652°W	7.96	55.00	21.70	n.d.
PG1-16	Z-II	21.61939°S	67.84614°W	8.18	52.40	21.30	5.85
PG1-15	Z-III	21.61928°S	67.84630°W	8.03	68.00	21.60	10.00
PG1-17	Z-IV	21.61947°S	67.84598°W	7.73	113.00	20.10	7.62
PG1-18	Z-IV	21.61949°S	67.84583°W	6.94	225.00	21.00	2.83
Wet conditions (March 2017)							
PG17-101	Z-Ia	21.61934°S	67.84835°W	5.8	26.7	40.9	8.29
PG17-102	Z-Ib	21.61936°S	67.84832°W	6.3	26.3	40.3	8.45
PG17-103	Z-Ib	21.61948°S	67.84824°W	6.65	26.9	39.4	11.02
PG17-105	Z-Ib	21.61954°S	67.84804°W	7.2	27.2	36.1	60.6
PG17-106	Z-II	21.61965°S	67.84732°W	8.12	27	24.6	3.21
PG17-107	Z-III	21.62001°S	67.84693°W	8.8	31.9	25	5.02
PG17-108	Z-IV	21.62012°S	67.84660°W	8.64	48	20.7	10.87
PG17-110	¹ CP	21.62035°S	67.84591°W	7.71	156.3	22.9	8.31

¹CP is an area of the carbonate platform flooded during the wet season (see Figure 5B).

Water samples from field investigations in January 2016 are reported in Table 3. They are moderately saline in Zones I and II ($15 \text{ g}\cdot\text{L}^{-1}$), and hypersaline in Zones III and IV (26 to $219 \text{ g}\cdot\text{L}^{-1}$). Ion concentration determined in La Salsa is much higher than in the ephemeral streams and freshwater Piedmont springs (See Table S1). Among the major chemical elements from the hydrothermal La Salsa spring, Na^+ and Cl^- are the most abundant, associated with K^+ , Ca^{2+} , Mg^{2+} , Li^+ , HCO_3^- , SO_4^{2-} , Si, and B (Table 3). As Cl^- is considered as a conservative element in water, it can be used to determine which elements precipitate along the downstream profile when the ratio of these elements decreases [63]. For the most abundant elements, Na^+ , K^+ and Mg^{2+} remain in solution and are removed in part in Zone IV, whereas Ca^{2+} , Mg^{2+} and HCO_3^- precipitate mainly in Zones III and IV. Si is removed all along the transect.

The computed saturation index from field investigations in January 2016 shows different behavior for amorphous silica and calcite along the transect (Figure 7f and Table 3). Amorphous silica is at equilibrium ($\text{SI} \sim 0$) in the central pool (Zone Ia), and is slightly oversaturated in the apron (Zone II), before becoming undersaturated in the distal zone (Zone IV). Calcite shows major changes. In the central pool, calcite is undersaturated ($\text{SI} = -0.24$), consistent with the absence of calcite precipitation. In the proximal and distal parts of the apron, calcite becomes oversaturated, with values above +0.5. In the distal zone, the calcite saturation index falls to +0.16, indicating a near-equilibrium state. Iron hydroxides, ferrihydrite $\text{Fe}(\text{OH})_3$, and goethite FeOOH are largely oversaturated all along the hydrothermal pathway, unlike gypsum, which is undersaturated.

4.2.2. Microbial and Mud Deposits

Microbial deposits are composed of nonmineralized microbial mats and microbialites. Six macroscopic morphologies were identified (Table 4), corresponding to facies F5, F6, and F7: ledges (F5), mushroom-like structures (F5), cerebroids (F5), snake-like structures (F6), isolated shrubs (F7), and planar shrubs (F7). Three mesoscopic fabrics were identified: planar-laminated, columnar-laminated, and clotted (Table 4). Microfabrics were divided into seven categories (Table 5): diatoms, ostracods, bundles of microbial sheaths, isolated microbial sheaths, peloids, micritic laminae, and siliceous laminae. Each morphology can be composed of one or more mesofabric and microfabric. For microbialites, elemental composition was determined from the central pool to the distal zone (Figure 7d,e, see Table S2). In microbialites bordering the central pool (ledge), both Ca/Si ratio and CaCO_3 content are low ($\text{Ca/Si} = 0.3$; $\text{CaCO}_3 = 47\%$). In the channel, both ledge and mushroom-like structures record a rapid increase in calcium ($\text{Ca/Si} > 2$; $\text{CaCO}_3 > 66\%$). These values then become relatively stable in the distal microbialites (cerebroids, snake-like structures, and shrubs).

Muds are essentially composed of a mixture of micritic aggregates associated to diatom frustules. Two types of mud were identified along the hydrothermal pathway, corresponding to part of facies F2: diatom mud (F2b) and ostracod-rich mud (F2c). The Ca/Si ratio and CaCO_3 content recorded in muds ($\text{Ca/Si} < 1$; CaCO_3 between 40% and 50%) are lower than in microbialites (Figure 7d,e, see Table 2), thus indicating a higher Si content. A marked change in mud composition corresponds to an increase in Ca/Si ratio (up to 1.6) and CaCO_3 content ($>75\%$), in the proximal part of Zone II.

Table 3. Chemical composition of La Salsa water sampled in January 2016 along the hydrothermal pathway. Reported values for chemical elements are in mg·L⁻¹. Columns associated with elements correspond to element/Cl⁻ ratio. SI indicates saturation index of a mineral.

Points	PG1-1		PG1-8		PG1-16		PG1-18	
Zone	Z-Ia		Z-II		Z-II		Z-IV	
pH	6.42		7.23		8.18		6.94	
Alkalinity (meq·L ⁻¹)	10.7		9.84		1.08		5.21	
Na ⁺	5063	5.53×10^{-1}	5073	5.59×10^{-1}	8816	5.50×10^{-1}	71,673	5.39×10^{-1}
K ⁺	523	5.71×10^{-2}	522	5.75×10^{-2}	936	5.84×10^{-2}	6809	5.11×10^{-2}
Ca ²⁺	457	4.99×10^{-2}	456	5.03×10^{-2}	589	3.67×10^{-2}	3093	2.32×10^{-2}
Mg ²⁺	132	1.44×10^{-2}	137	1.51×10^{-2}	224	1.39×10^{-2}	1571	1.18×10^{-2}
SO ₄ ²⁻	283	3.09×10^{-2}	270	2.97×10^{-2}	498	3.11×10^{-2}	2941	2.21×10^{-2}
Cl ⁻	9147	-	9068	-	16,028	-	133,044	-
HCO ₃ ⁻	381	4.16×10^{-2}	591.4	6.52×10^{-2}	173.4	1.08×10^{-2}	237.8	1.78×10^{-3}
Li ⁺	69	7.54×10^{-3}	71	7.83×10^{-3}	113	7.05×10^{-3}	789	5.9×10^{-3}
Sr ²⁺	9.7	1.06×10^{-3}	9.8	1.00×10^{-3}	15	9.3×10^{-4}	111	8.34×10^{-4}
Ba ²⁺	0.19	2.07×10^{-5}	0.23	2.53×10^{-5}	0.38	2.37×10^{-5}	1.7	1.27×10^{-5}
Fe	0.17	1.86×10^{-5}	0.08	8.82×10^{-6}	<0.04	-	<0.04	-
B	35	3.82×10^{-3}	35	3.86×10^{-3}	64	3.99×10^{-3}	396	2.97×10^{-3}
Si	72	7.87×10^{-3}	67	7.38×10^{-3}	62	3.86×10^{-3}	30	2.25×10^{-4}
Br ⁻	4.8	5.24×10^{-4}	4.7	5.18×10^{-4}	8	4.99×10^{-4}	61	4.58×10^{-4}
SI _{Amorphous. silica}	-0.01		0.06		0.08		-0.07	
SI _{Calcite}	-0.24		0.61		1.48		0.16	
SI _{Fe(OH)3 (2L)}	1.83		2.57		3.09		0.98	
SI _{FeOOH}	4.70		5.51		6.18		4.12	
SI _{Gypsum}	-1.27		-1.68		-1.59		-0.59	

Table 4. Macrofabrics of the microbial deposits.

Macrofabric	Composition	Structure	Dimension	Biological Community	Substrate	Depositional Environment	Zone and Facies
Ledge	Alternating laminae composed of micrite, bundles of microbial sheaths and diatoms, coating F4. The upper and lateral parts of the structure show a transition from bundles of microbial sheaths to micritic laminae, sheltered parts infilled by diatoms and ostracods	Planar laminated structure; growth in stairs	2 to 5 cm thick; 5–20 cm long	Green mat; diatoms	F4	Central pool and channel	I, F5
Mushroom-like		Planar to curved laminae	5–10 cm in diameter	Green mat; diatoms	F4	Channel	I, F5
Cerebroid	Alternating laminae composed of micrite, bundles of microbial sheaths and diatoms, coating F4. The upper and lateral parts of cerebroids show a transition from bundles of bacterial sheaths to micritic laminae, bundles composed of cast and mold of filaments	Irregular ovoid structure, composed of planar and columnar laminae	2 to 20 cm in diameter	Green mat; diatoms	F4	Apron	II, F5
Snake-like	Alternation of densely packed and loosely packed micritic peloid laminae with diatoms, top structure showing siliceous cements and gypsum	Laminated and clotted hemispherical and tortuous structures showing a white crust on their upper part; white crusts locally covered by mm micrite and silica-rich branches	10 cm to 1 m long	Black mat; diatoms	Associated with F2b, resting on F1	Transitional proximal–distal belt	III, F6
Isolated shrub	Alternation of micritic to sparitic laminae, and siliceous laminae, coating F1. Transition from F1 to shrub laminae is marked by a corroded surface coated with iron oxides. Microstalactitic cements precipitating between downward-facing microstromatolites.	Planar to columnar (finger-like) structures	2 to 5 cm in diameter	Black mat; diatoms	F1	Distal zone	IV, F7
Planar shrub		Planar, with columnar structure at the edges, and with a smoothed central part	Ranging from 5 cm to 50 cm	Black mat; diatoms	F1		IV, F7

Table 5. Microfabric description and associated macrofabrics.

Microfabric Components	Main Characteristics	Description	Size	Macro	Zone
Diatoms	-	Accumulation of well-preserved or fragmented diatoms organized in clusters or layers, or observed as mats (slime)	10 to 150 µm	Accumulation as layers or trapped in ledge, mushroom-like, cerebroid, snake-like morphologies	I, II and III
Ostracods	-	Clusters composed of ostracods associated with diatoms, micrite, and iron hydroxide, infilling dissolution cavities or trapped within microbial or diatomaceous layers, complete and disarticulated ostracods	200 to 600 µm	In association with mushroom-like and cerebroid morphologies	I, II and III
Micritic aggregates	-	Aggregates of micritic crystals incorporating diatoms	20 to 500 µm	Diatomaceous mud	I, II and III
Microbial sheaths	Bundles	Microbial sheaths organized in bundles and associated with diatoms, preserved as internal fossil molds embedded with micrite or as filament casts filled by Fe–(Mg–As) silicate gel	Bundles up to 2 mm; more than 2 mm width molds 7–10 µm in diameter and over 200 µm long; Casts 13–20 µm in diameter and up to 300 µm long	Bundles developed on hard substrate (previous growth phases) organized in ledge, mushroom-like and cerebroid morphologies	I and II
	Isolated	Single microbial sheaths embedded in micritic peloids Well-preserved casts of filaments filled by Fe silicate gel	13–17 µm in diameter and up to 300 µm long; rare broken fragments	Isolated microbial sheathss incorporated in snake-like and shrub morphologies	III and IV
Peloids	–	Irregular micritic peloids organized in clots; their density can vary, forming darker or lighter layers with associated diatoms or calcite/silica cement	100 to 200 µm; can exceed 1 mm	Accumulation of peloids in snake-like morphologies	III
Laminae	Micritic and micritic to sparitic	Irregular or continuous wavy to planar micritic laminae (microbial origin?)/transitional micritic to sparitic laminae	30 to 500 µm	In ledge, mushroom-like, cerebroid, and shrub morphologies	I, II and IV
	Siliceous	Thin discontinuous laminae of amorphous silica	20 to 200 µm	In shrubs	IV

Biological activity is present throughout the hydrothermal spring system. Three main biological communities were differentiated based on morphological observations of mats in the field: green microbial mats, black microbial mats, and diatoms. A common feature throughout La Salsa is the abundance of diatoms and bacteria usually embedded in Extracellular Organic Matter (EOM), the main site for mineral precipitation [64–66]. Both diatoms and bacteria are associated in all mat types, either as main producers, or trapped in the EOM. Green mats are typically subaqueous, forming dense planar mats a few centimeters thick, with cyanobacteria filaments up to 5 cm long (see Figures 8C and 9B). Black pustular mats display various morphologies, from pustular to wavy or wrinkled, from a few millimeters to 5 centimeters thick, encrusting oncoids, shrubs, and carbonate crusts (see Figure 12A,B). They grow close to the air–water interface and are subject to desiccation. Black pustular mats are composed of bacterial filaments and associated coccoids. No specific characterization is available for microbial communities in Pastos Grandes, but the black pustular mats show similarities with those described at Laguna Negra in Argentina [66,67]. Diatoms are accumulated and associated with slime (EOM and organic matter) in shallow waters (>2 cm deep), and their frustules are observed in every active zone of the hydrothermal system. They are commonly classified as planktonic (i.e., suspended, unattached in open water), benthic (i.e., living on the bottom of the lake floor), or periphytic (i.e., attached to substrates such as stones, aquatic vegetation, and sand). Diatoms are common on the Altiplano, and the Pastos Grandes Laguna displays a large variety of pennate species, with a distribution responding to several environmental factors (water chemistry, temperature, salinity, pH, and depth) [27,68].

4.2.3. Zonation of the Depositional Environment

Zone I—The Hydrothermal Feeding System

The hydrothermal feeding system is divided into two subzones: the central pool (Subzone Ia) and the outflow channel (Subzone Ib). Subzone Ia presents a large basin, 28 m long, 12 m wide, and approximately 1.2 m deep, hosting the vent (Figure 8A). Although no vent chimney is visible, surface agitation with bubbles indicates where hot water (42 °C) and CO₂ (75%), N₂ (22%), and O₂ (3%) emerge [29]. The suspended sediment load retrieved by filtration contains diatom frustules and fine calcite grains (Figure 8B). Approximately half of the pool is rimmed by a microbial, diatomaceous bindstone (F5), which forms an overhanging ledge at the air–water interface (Figure 8C). Ledges are composed of planar alternations of micritic calcite, bundles of microbial sheaths (up to 500 µm), and diatom accumulations (Figure 8D,E). Green mats covering these ledges may extend up to 10 cm over the pool, when agitation is low (Figure 8C). Ledges transition laterally to pedogenic packstones-floatstones (F4). Pedogenic packstones-floatstones (F4) and ledges (F5) both overlie the cohesive mud (F2a) of the proximal flat mound. Locally, diatom mud (F2b), containing Fe oxides, lines the pool walls. No ledges are present on the northwestern side of the pool, with a large flat zone, usually submerged by very shallow waters, and simply covered by diatom mud (F2b). Water flows out southeastward through a single channel (Subzone Ib), over a distance of 50 m. This channel is approximately 0.5 to 1 m wide, broadening midstream (Figure 9A). It incises approximately 20 cm into the flat mound, revealing intraclasts of pedogenic packstones-floatstones (F4). The edges of the channel are generally rimmed by ledge microbialites (F5), occasionally colonized by green mats, with poor lateral extension. The channel floor is covered by a few centimeters of cohesive ostracod-rich mud (F2c), which evolves from brown to black along the pathway, and is often covered by dense green microbial mats (Figure 9A). A second type of microbialite, defined as mushroom-like (F5b), is observed in the stream flow (Figure 9B). These microbialites are uncommon and grow on pedogenic packstones-floatstones (F4). They show the same internal organization as ledges (F5), with alternating laminae of micrite, bundles of microbial sheaths, and diatoms (Figure 9C). Bundles of microbial sheaths may be embedded in calcite mineralization (Figure 9D), and in silicate gel mineralization (Figure 9E). They expand laterally into flat-topped structures as they reach the air–water interface. The top of these

mushroom-like structures shows accumulations of ostracod-rich mud (F2c), with diatom frustules, ostracod shells, calcite clusters, and silicate gel (Figure 9F,G).

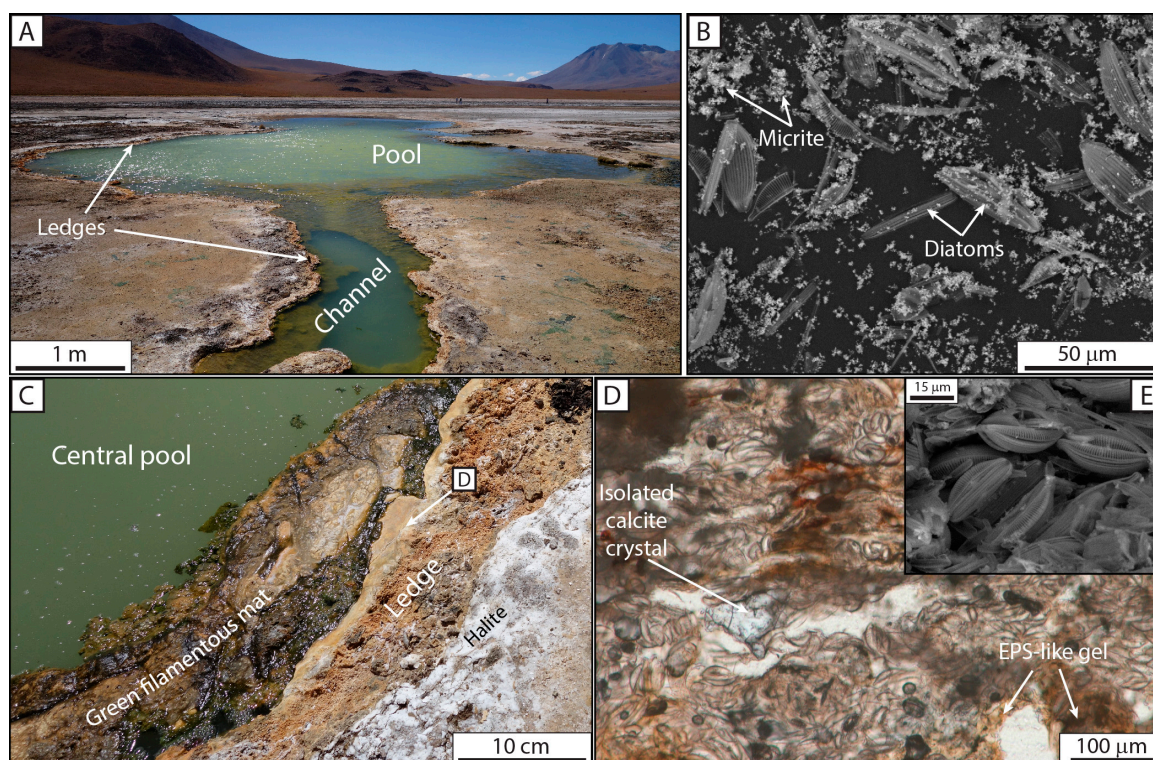


Figure 8. Illustration of the central pool in La Salsa (Zone Ia). (A) View from the southeastern part of the pool and its perennial outlet: the channel (Zone Ib). (B) The SEM image of the suspended sediment load in a 1 micron filter of water sampled at the border of the central pool, containing well-preserved diatoms and very fine calcite crystals. (C) Field view of overhanging ledge microbialites developing from the pool edges. (D) The PPL view (thin section) of a ledge microbialite, showing abundant diatoms, with brown EPS, and an isolated sparite crystal. (E) The SEM view of these well-preserved pennate diatoms.

Zone II—The Apron

After a relatively short straight trajectory in the outflow channel, thermal waters disperse over the apron (Figure 5B). This zone is characterized by an anastomosed pattern, where the flow path disperses in shallow streams (up to 10 cm deep), between elongated ridges of ostracod-rich mud (F2c; Figure 10A). These ridges, approximately 50 cm, to more than 200 cm, long, and 20 to 60 cm wide, are generally oriented along the gentle slope of the hydrothermal mound. Macroscopic observations and SEM analyses show that these ridges contain coarse intraclasts, inherited from the underlying carbonate platform (F1a, F1b), mixed with ostracod-rich mud (F2c). This mud is composed of fragmented and nonfragmented diatoms, ostracods, and small micritic aggregates (Figure 10B). Downstream in the apron zone, ostracod-rich mud (F2c) is associated with microbial and diatomaceous bindstone, forming scattered indurated cerebriform structures (F5; Figure 10C). These cerebriform microbialites grow on reworked clasts composed of pedogenic packstones-floatstones (F4), and blocks inherited from the carbonate platform (F1a, F1b). Similarly to mushroom-like microbialites (F5), cerebriforms tend to enlarge upward, becoming discoidal in shape when they reach the air–water interface. Thin sections show a similar composition to ledges and mushroom-like structures, with alternations of micritic, microbial-rich, and diatomaceous laminae. However, they differ in organization, with planar-laminated micritic-rich layers, locally transitioning to columnar-laminated layers. Microbial sheaths observed over micritic layers are organized in bundles, from 500 μm to 1 mm long. Laminae are sometimes

crosscut by erosional surfaces (Figure 10D), and the resulting dissolution cavities are rimmed and infilled with ostracod-rich mud (F2c).

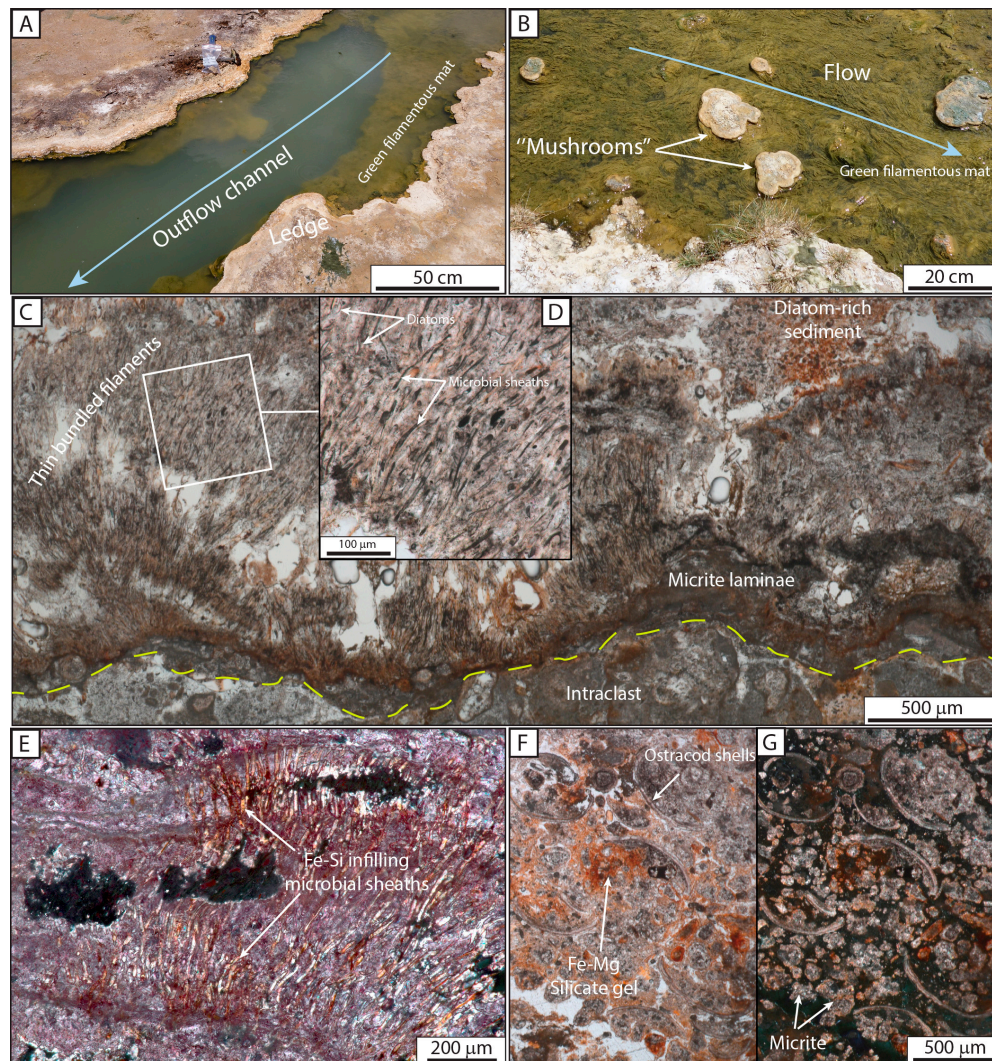


Figure 9. Illustration of the channel facies (Zone Ib). (A) Overview of the channel with overhanging microbialite ledges and submerged green mats. (B) Mushroom-like microbialites growing in the stream, among green mats covering the channel floor. (C) The PPL view of a mushroom-like microbialite growing on an intraclast (lower part of the view). The eroded intraclast surface (dashed yellow line) is successively encrusted by micritic laminae, bundles of microbial sheaths, and diatom-rich sediment. The bundles of microbial sheaths and the diatom-rich laminae are cemented by calcite and locally glued with brown EPS. (E) The PPL view of AF-stained coarse microbial sheaths organized in bundles. Sheaths are cemented by calcitic microspar. (F,G) The PPL and XPL views of sediments covering the top of mushroom-like microbialites, consisting of a mixture of ostracod valves, micrite/microspar clusters, diatoms, and rust-colored silicate gels containing Fe and As.

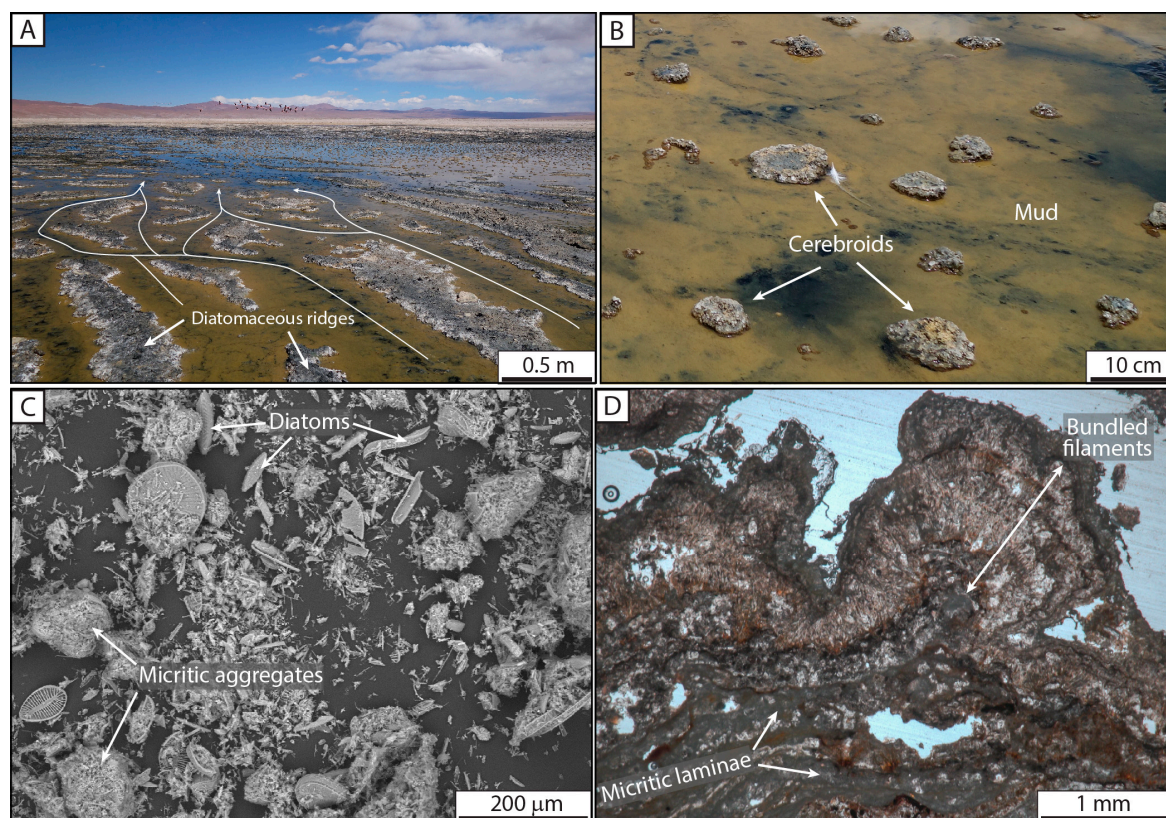


Figure 10. Illustration of the apron (Zone II). (A) Overview of the apron with diatomaceous ridges bordering anastomosed channels filled by mud. (B) Cerebroid microbialites dispersed over the muddy sediment of the apron floor. (C) The SEM view of mud covering the apron floor, with micrite aggregates and diatoms (well-preserved or fragmented). (D) The PPL view of a cerebroid microbialite, showing several micritic laminae capped by thick laminae of bundles of microbial sheaths.

Zone III—The Proximal–Distal Transitional Belt

The distal part of the apron transitions to a flat zone, corresponding to an increase in preserved microbial deposits (Figure 5B). Soft sediment covers almost all the surface of Zone III, forming numerous small snake-like structures (F6; Figure 11A,B), which are sometimes laterally associated with ostracod-rich mud (F2c). At microscale, F6 is composed of dense or more loosely packed layers of clotted micrite, displaying microbial sheaths and diatoms (Figure 11C,D). These sinuous structures (5 to 10 cm wide and up to 1 m long) emerge from the water, and the exposed parts display a poorly lithified white crust (Figure 11A). This superficial whitening is identified as amorphous silica and gypsum (Figure 11E). Some crusts capping the snake-like structures even show a dense network of millimetric branches mimicking the shrub-like structures of Zone IV (Figure 11B). Locally, their edges are covered by black microbial mats. These structures are often modified by desiccation cracks.

Zone IV—The Distal Zone

Zone IV corresponds to the distal part of La Salsa, where thermal waters progressively come into contact with the carbonate platform (Figure 5B). The aerial view shows a complex black and white patchwork (Figure 5B), composed of whitish shrubs (F7), and poorly to nonmineralized black microbial mats, up to 5 mm thick, developed on both shrub and mud facies. Microbial mats present three morphologies: wavy, wrinkled, and pustular, with the pustular morphology being the most common (Figure 12A). Microbial mats are frequently observed underwater, or close to the air–water interface. Mineralized shrubs (F7), distinguished by their millimetric branches [69], dominate the white parts of Zone IV (Figure 12B–D). These shrubs often grow directly on corroded and dissolved

fragments of the carbonate platform (F1a–c). At microscopic scale, shrubs are composed of laminar alternations of micritic and sparitic calcite and opal-A laminae, including rare diatoms (relatively less abundant than in other facies). Locally, these laminar mesostructures become columnar mesostructures (Figure 12E). During precipitation, some microbial filaments can be trapped on or inside the shrubs (Figure 12F,G). Micritic laminae may laterally become sparitic at the edges (Figure 12H). This transition is also observed in the topmost part of the shrubs. At the bottom, sparry calcite can also develop between the branches, usually forming microstalactitic cement (Figure 12I). Shrubs are preserved as isolated forms (1 to 5 cm), or planar forms (5 to 50 cm), particularly in the most distal parts of Zone IV. Locally, these slabs are broken and tilted, and may be partially covered by discordant ostracod-rich mud (F2c), or a new generation of shrubs (Figure 12C). In the northeastern part of Zone IV, shrubs are locally aligned in rims, especially above fractures in the underlying carbonate platform. These rims surround large, shallow pools, colonized by black pustular mats, where water flows north toward a slightly depressed area of the platform (see Figure 5B).

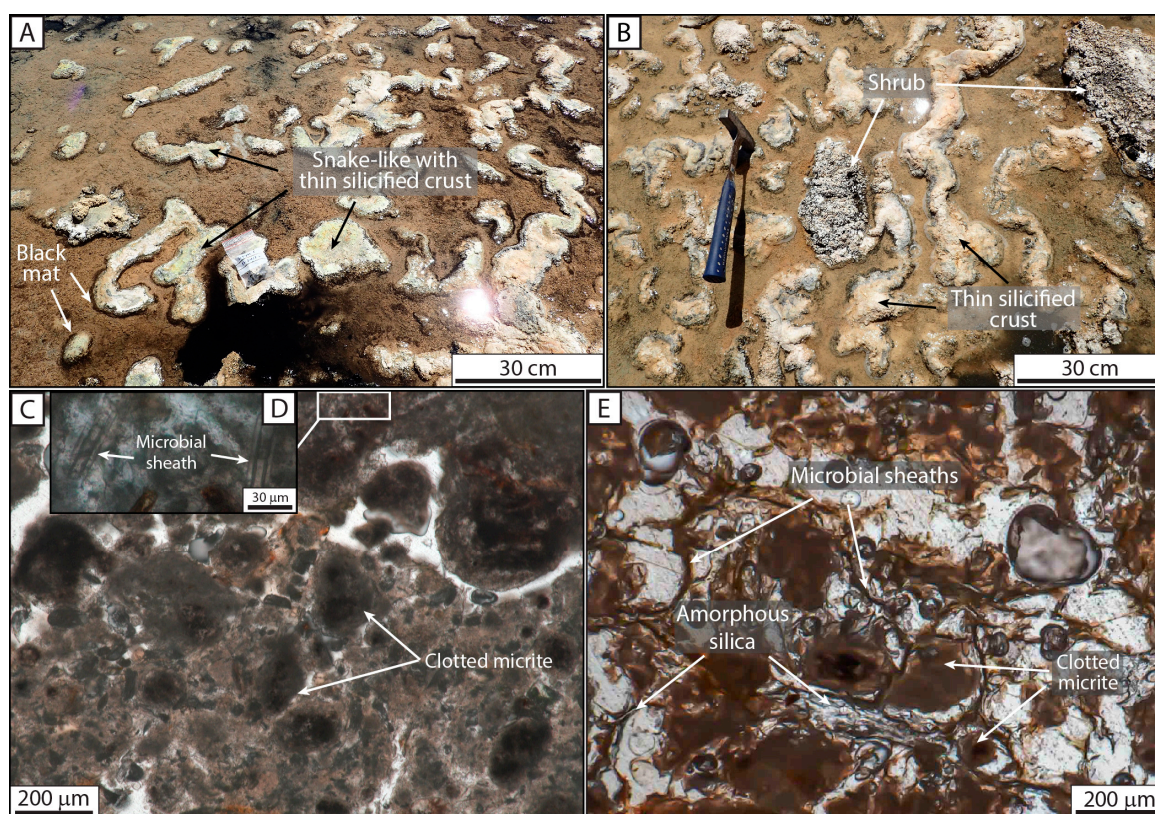


Figure 11. Illustration of the proximal–distal transitional belt (Zone III). (A) Field view of snake-like structures marked by very thin crusts of white amorphous silica, developing on the dewatered parts, and surrounded by discontinuous black microbial mats. A brownish diatom-rich labile slime develops on the muddy floor. (B) Other snake-like structures, again with thin white silica crusts. On higher emerged asperities, the first developments of shrub microbialites, with Si- and Ca-rich laminae (see Zone IV). (C,D) The PPL views of the cohesive sediment forming the snake-like structures. It contains poorly cemented clotted micrite, with occasional microbial sheaths (close-up view D). (E) The PPL view of the thin siliceous crust covering the snake-like structures. Clotted micrite and microbial sheaths are encrusted by amorphous silica.

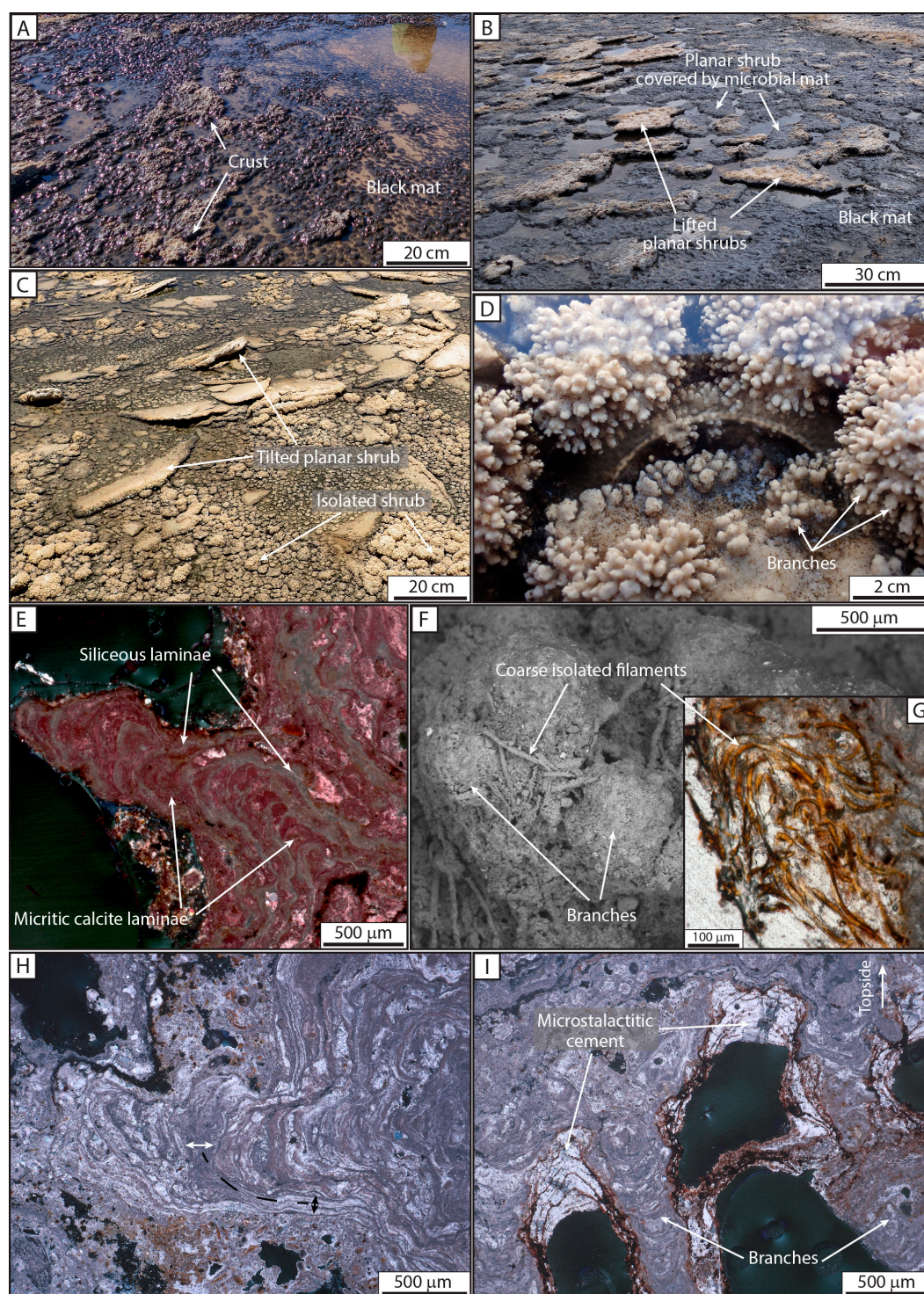


Figure 12. Lithified facies of the distal zone (Zone IV) observed and sampled in dry conditions. (A) A black pustular mat locally emerging, displaying carbonate and siliceous crusts with small branches. (B) Thick black wavy mats associated with planar shrub slabs. Some are slightly lifted up, marked by the disappearance of the black mat resulting from longer aerial exposure. (C) Coexisting isolated and planar shrubs in the distal part of Zone IV. Black pustular mats are thin and discontinuous, restricted

to deeper pools. (D) Close-up view of isolated underwater shrubs. (E) The XPL view of a shrub branch. The AF-staining reveals laminae of irregular thickness, alternating between micrite (in red) and amorphous silica (in gray), forming a branch-like, columnar structure. Nonferrous blocky calcite cement also precipitates between the laminae. (F,G) The SEM and PPL views of coarse isolated microbial sheaths around shrub branches, respectively. Sheaths are filled by a brown silicate gel. (H) The XPL view of a shrub branch composed of micrite–sparite alternations. Micritic laminae mainly develop at branch extremities, whereas sparitic laminae are thicker on lateral parts of branches. (I) The XPL view of downward-facing branches, with microstalactitic sparite cements (vadose) precipitating between them (the arrow indicates the top of the shrub). Note also the presence of thin iron-rich laminae.

The Transient Peripheral Saline Zone

A transient zone can be identified at the boundary between the distal zone of La Salsa and the carbonate platform. During rainy episodes, a mixture of rainfall and La Salsa spring water submerges the lower areas of this zone. As observed in March 2017, such floods last only a few days, thus preventing microbial mat formation and microbialite development. However, when they evaporate, these mixed waters leave a thin layer of halite over the carbonate crust (F1a–c), as observed in January 2016.

5. Interpretation and Discussion

Hydrothermal springs related to volcanism are generally fed by Si-rich fluids, with deposits mainly dominated by silica in the form of opal-A [2,12,70,71]. The hydrothermal La Salsa sedimentary system is fed by a great diversity of ions, with CO₂ inputs. It displays unusual characteristics, with a flat mound, and both calcite and silicate deposits. The discussion will focus on the processes leading to mound formation, the main parameters controlling facies distribution and microbialite fabrics along a hydrothermal pathway, and the respective roles of biotic versus abiotic factors in Ca-Si mineralization.

5.1. Origin of the Flat Mound

Mound morphologies associated with hot springs are diverse, ranging from flat mounds to chimney morphologies [70,72]. These morphological differences result from several parameters, including surface topography, hydrostatic head, flow rate, and the degree of oversaturation of minerals at the vent [72]. In a slope setting, the hydrothermal flux tends to build terraces and pools, bounded by dams where mineral oversaturation is easily reached [19]. In La Salsa, the flat regional topography of the Pastos Grandes Laguna, the moderate flow rate, and the low degree of oversaturation at the vent easily explain the resulting flat mound morphology of the hot spring, with a slight northeasterly slope, as indicated by the propagation of major hydrothermal mound deposits in that direction.

Currently, the flat mound is inactive, but still remains under the influence of surface processes. The distal rims and channels along the mound flanks are affected by intense pedogenesis [62], as indicated by the presence of pedogenic packstones-floatstones (F4). The flat mound is also modified by cryoturbation and desiccation processes, progressively erasing the structure of rims and channels, arguing for older developmental stages. Cryoturbation is best illustrated in the apron by the presence of diatomaceous ridges, incorporating intraclasts from the carbonate platform. Clustering of intraclasts is commonly observed in periglacial structures resulting from reworking by freeze–thaw processes [73]. Ridge structures observed here resemble the stone stripes formed of size-sorted stones grouped along slopes [74,75], often observed in high altitude and/or latitude areas. The composition of the ridge structures here is different, however, as mud is more dominant than stone in the hydrothermal La Salsa system. Kessler and Werner [76] modeled the impact of slope and stone density on particle organization, producing elongated structures along the slopes, with patches when stones were less dominant. The results obtained from their model are similar to the diatomaceous ridges containing platform intraclasts observed in the apron.

Clearly visible rims and channels are concentrated around the central pool, and are episodically flooded. Satellite images confirm that episodic overflows occur throughout the year, feeding ephemeral channels crossing the mound flanks. These channels are related to hydrological changes resulting from rainfall (wet season) or snowmelt (dry season). However, seismic activity can also trigger changes in the hydrologic response of hydrothermal springs [77,78], but no data currently support this hypothesis. The episodic increase in the surface area of the mound under flooding may favor the accumulation and precipitation of sediments. The mound was most probably formed by the accretion of mud-dominated sediments. Diatoms typically produce a large amount of exopolymeric substances (EPS) as protection against hydric stress and changes in salinity [79], both of which factors are present in the hydrothermal La Salsa system. In association with overflows, diatom mats may extend laterally on to flooded flat areas around the central pool, but also favor carbonate precipitation as pH increases further from the pool, promoting the development of aggregates. This in situ production of diatom- and microbial-rich carbonate aggregates, during repeated ephemeral flooding of the mound flanks, favor the accumulation of soft sediments, resulting in the flat geometry of the mound. Ephemeral flooding also prevents the development of mineralized microbial structures, which are only preserved in constant water-fed domains, as observed in the central pool and downstream areas.

Mineral precipitation also occurs within sediments, as shown by the crystallization of aragonite needles, especially below the water table (Figure 6E). These needles grow around aggregates and diatoms, indicating a diagenetic origin in the phreatic zone. This authigenic mineralization does not result in mud lithification, but may trigger the swelling of unconsolidated sediments. At the surface, this swelling appears as a slight uplift, maintaining or amplifying the flat mound morphology. Authigenic processes in hydrothermal settings are well known: one such well-studied case concerns thermogenic mounds and ridges above Little Grand Wash and Salt Wash normal faults in central Utah, USA [80,81]. There, the rapid growth of numerous authigenic aragonite crystals within extensive horizontal veins in the sediment is able to uplift the overlying sediments. Uplifts have also been observed in several marine mud deposits, in association with generations of cementation and possible brecciation [82–84].

Authigenic mineralization and biotic accumulations are more plausible processes for flat-mound formation, even though several observations (e.g., depression around the mound and muddy sediments) might also indicate mud volcanism as a potential factor [85,86]. The peripheral depression observed around the flat mound (Figure 13A), and around several smaller hydrothermal mounds (Figure 13B), could be a consequence of shallow-layer reworking resulting from seismic activity [87,88], well-described process triggering liquefaction of buried sediments [89–91] and mud volcanism [86,92,93]. Despite, Seismic activity occurring around the surrounding of the Pastos Grandes caldera which could have triggered liquefaction (See Figure S1), the past 35 years of satellite images provide no evidence of mud volcanic activity on the hydrothermal flat mounds (Credit: U.S. Geological Survey, Landsat Product). Hydrothermal emissions are relatively clear, with a low particle charge in the central warm pool (below 43 °C), consisting of free micritic grains, and grains nucleated on recently deposited diatom frustules (Figure 8B), suggesting in situ formation. The presence of subsurface layers enriched in micritic aggregates (F2a) below the hydrothermal La Salsa system therefore remains unconfirmed. Diagenesis occurring with aging [94], and enhanced by water circulation [95], strongly affects the opal-A of diatom frustules, modifying their initial texture [95,96]. Diatom frustules are also sensitive to salinity conditions, which favor their dissolution [97,98]. Salinities recorded at La Salsa are close to or higher than the estimated threshold value (20 g·L⁻¹) above which the diatom record is modified [98]. The buried sediment reworking hypothesis is thus not coherent with the preservation of opal-A mineralogy of diatom frustules observed in La Salsa.

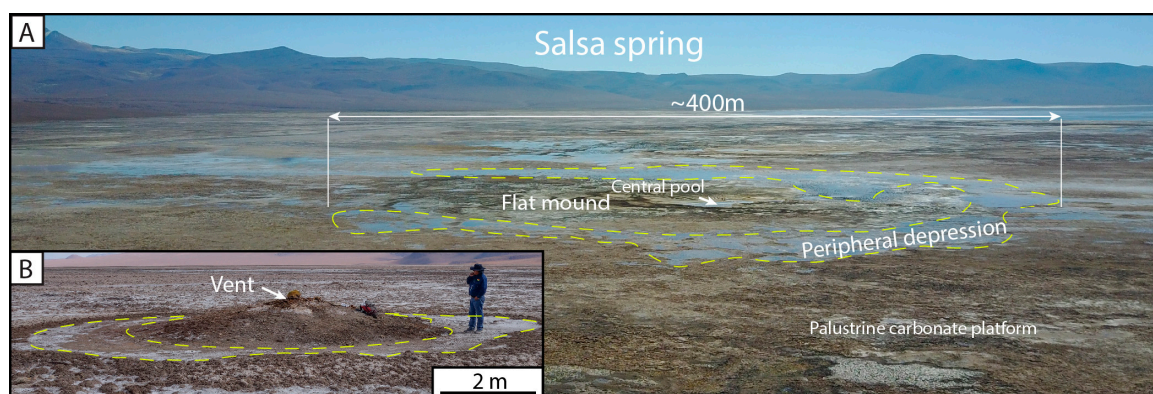


Figure 13. Peripheral depressions around several Pastos Grandes hydrothermal mounds. (A) Drowned peripheral depression around the flat mound in La Salsa during the wet season (March 14th, 2017). (B) Dry depression, partially filled by halite, surrounding a small hydrothermal mound capped by iron-rich encrustation around the vent. Dry episode, northern part of the carbonate platform (−21.59466 N; −67.83755 E).

5.2. Interaction between Microbialites and their Physical Environment

Mound morphology induces a nonrandom distribution of microbial deposits (Figure 7b). Microbialite morphologies (i.e., ledge, mushroom-like, cerebroid, snake-like, isolated shrub, and planar shrub) present specific distributions along the entire La Salsa transect. Several extrinsic factors (i.e., accommodation, hydrodynamics, and substrate) can determine microbialite distribution, abundance, and morphologies (Figure 14).

Accommodation space is a major driving factor, particularly in marine and lacustrine contexts, as variations in water depth constrain microbial mat development, thus affecting microbialite size and morphology [99–102]. In hydrothermal systems, accommodation space mainly depends on water discharge (i.e., hydrothermal input and rainfall) and fluid upwelling [103]. As a consequence, in palustrine domains, accommodation space is relatively low along the hydrothermal pathway of La Salsa (<10 cm, except in the central pool), limiting microbialite size to a few centimeters in height. Accommodation space is therefore unlikely to be the only factor controlling microbialite morphology in La Salsa.

Hydrodynamics also has an impact on microbialite macrofabrics and mesofabrics [100,101,104]. In hydrothermal springs, hydrodynamics may be related to the relative angle of the slope (e.g., flat mound), triggering variations in flow rate. In La Salsa spring, a hydrodynamic gradient is identified by (1) wind bursts and swirling in the central pool, (2) a higher flow rate in the channel, decreasing in the apron, related to the slight slope of the flat mound, and (3) stagnant water in the transitional belt and the distal zone. Swirling within the pool creates turbidity, particularly at the vent (Figure 3A), which is not favorable to the presence of microbialites at depth, as it reduces brightness, thus disfavoring photosynthetic communities. Ledge morphologies are found around the pool and channel edges. This type of edging is common in siliceous sinters [1,15,70], travertines [19], and even in marine lagoonal environments [101]. Swirling and high flow rate increase air–water exchange, CO₂ degassing, and mineralization. These factors, coupled with a constant water level, as observed by Renaut et al. [19], favor the lateral growth of ledge and mushroom-like morphologies. On reaching the apron (Zone II), waters pour over a larger unrestricted area, triggering a decrease in flow rate, with more irregular cerebroid growth. In the transitional belt and the distal zone, waters become stagnant, and strong evaporation conditions prevail, leading to encrustation and microstromatolite formation. However, hydrodynamic factors do not explain the difference between snake-like and shrub morphologies.

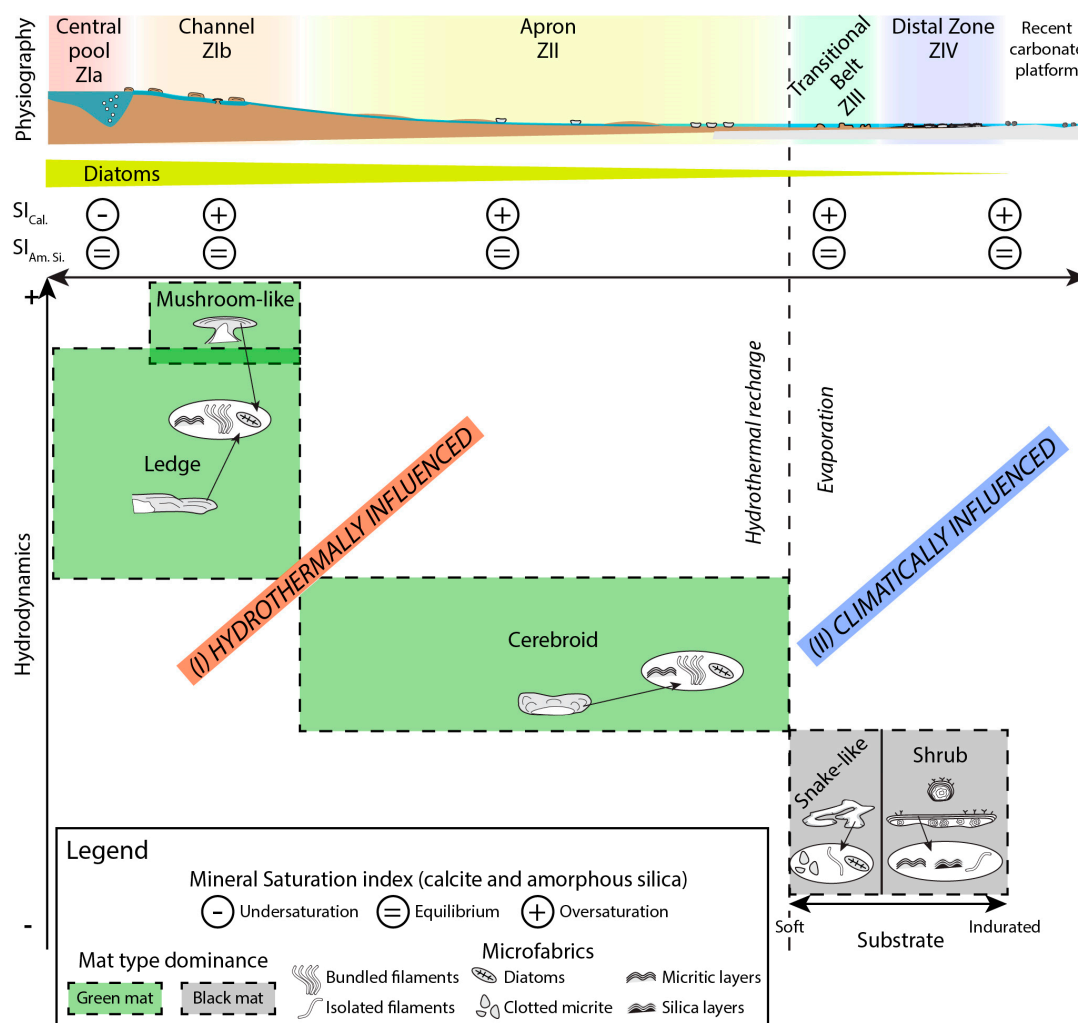


Figure 14. Sketch showing the distribution of microbialite morphologies along the hydrothermal pathway, in relation to hydrothermal input, climatic fluctuation, and hydrodynamics. (I) Green mats proliferate under hydrothermal influence (proximal Zones Ia, Ib, and II), favoring ledge, mushroom-like, and cerebroid microbialite development, together with mud deposits. Mushroom-like microbialites are constrained by relatively high hydrodynamics, while cerebroids are constrained by lower hydrodynamics. Ledges are less affected by hydrodynamics, whether moderate (central pool) or high (channel). (II) Black mats are found in distal Zones III and IV, submitted to drastic daily-to-annual climatic variations (temperature, wind, and precipitation). These conditions favor the growth of snake-like structures on soft sediments and shrubs on the indurated substrate.

The low abundance of microbialites in the median part of the system (the apron), and their intense development upstream (pool and channel edges), and downstream (transitional belt and distal zone), seem to be related to the nature of the substrate on which the microbial deposits grow. The role of the substrate in microbialite morphology and distribution is seldom discussed in the literature, but some studies highlight the importance of an indurated substrate for microbialite initiation [105–108]. At microscale, some authors [109,110] have shown that the substrate plays a role in mineral precipitation, and the resulting microfabrics (e.g., laminar fabric on continuous substrate and peloidal or dendrolitic fabrics on organic fragments and cyanobacterial filaments). Roche et al. [111] suggested that microbialite development requires fundamental elements for precipitation, such as water oversaturation in a specific mineral, and a suitable substrate for microbial mat fixation and mineralization. In the hydrothermal La Salsa system, substrates are divided into hard substrates

(i.e., pedogenic carbonate crust, and inherited carbonate platform fragments), and soft substrates (i.e., mud, and microbial mats).

Ledge morphologies develop on steep edges, where indurated surfaces are observed, sometimes producing a continuous rim. Indurated surfaces identified as pedogenic packstones-floatstones result from the cementation of underlying unlithified muds and carbonate platform clasts [107]. Ledge morphologies cannot develop where edges are flatter, or covered by mud, thus preventing the formation of microbial mats and microbialites. Mushroom-like microbialites are scarce in the channel, where the substrate is composed of soft sediments, and develop only on the substrate of pedogenic packstones-floatstones. Scattered cerebroids are observed on the soft ostracod-rich mud in the apron, developing from pedogenic or carbonate platform fragments. By contrast, in most cases, recent accumulations of soft mud do not lead to microbial mat development. However, in Zone III, snake-like microbialites develop in association with mud sediments, possibly because of strong evaporation in this zone during arid periods, which could lead to partial drying-up, inducing mud lithification, and therefore microbial mat development. Similar substrates have been identified in Bahamian deposits, with microbialites developing on firm ground [107,112]. However, the limited growth of snake-like structures indicates that lithification is relatively low [113]. In interconnected stagnant shallow water ponds in the distal zone, numerous pisolites and carbonate platform fragments can lead to the formation of isolated or planar shrubs. As the same stagnant conditions exist in Zones III and IV, the main difference in microbialites probably results from the nature of the substrate, with snake-like morphologies on soft sediments and shrubs developing on hard substrates. A stable hard substrate thus appears to be a major factor controlling the shape and spatial distribution of microbialite deposits [101,105,114,115].

5.3. Controlling Factors in the Development of Biotic/Abiotic Products

Despite the impact of flat-mound morphology on microbialite distribution, the similarities and differences observed in microbialite microfabrics in different zones cannot be simply the result of physical controls. Changes in the pattern and intensity of mineralization were observed in different microbialites with the same microfabrics, and in different microfabrics with the same microbial structures. Microfabrics result from the interaction of biological activities (diatoms, green mats, and black mats) and from fluctuations in physicochemical parameters that modify the amorphous silica/calcite balance.

The microfabrics observed in Zones I to II (ledges, mushroom-like structures, and cerebroids) are very similar, but with major changes in the Ca/Si ratio. At the pool edges in La Salsa (Zone Ia, $T < 43\text{ }^{\circ}\text{C}$), the amorphous silica saturation index is at equilibrium (Figure 7f), suggesting that aqueous silica, arriving in excess from the hydrothermal vent, is constantly removed from the solution. In general, diatoms develop in hot springs when the temperature falls below $45\text{ }^{\circ}\text{C}$, and they increase in diversity as the water temperature cools [116–118]. Silica is mainly found in diatom frustules, either trapped in green microbial mats or accumulating in irregular diatomaceous layers, and thus participates in microbialite growth [119]. The equilibrium obtained for the silica saturation index may be related to its immediate consumption by diatoms, and the availability of aqueous silica in the pool is probably a factor limiting diatom development. Despite a negative calcite saturation index (Figure 7f) in the free water of the pool, the CaCO_3 content of mineralized microbialites reaches 47%, indicating that equilibrium is reached locally in the wall of the pool. Thin sections (Figure 8D) and micro-XRF mapping (Figure 15A) reveal that CaCO_3 content corresponds to micritic clusters and blocky calcite cements. Clusters are probably the result of local microbial activity in mats [65,120], while cements are related to very early diagenesis in dewatered parts of the mats. Locally, the abundance of diatoms and cyanobacteria can increase pH, due to their high level of photosynthetic activity, thus favoring carbonate precipitation in the mat [28,121]. The high Fe content in microbialites recorded in Zone I (Figure 15) can be explained by the rapid formation of iron hydroxides or hydrous iron silicate, through

the oxidation of reduced iron transported to the pool by the hydrothermal waters, coherent with the low Fe concentration in water, and the high iron hydroxide saturation index [122].

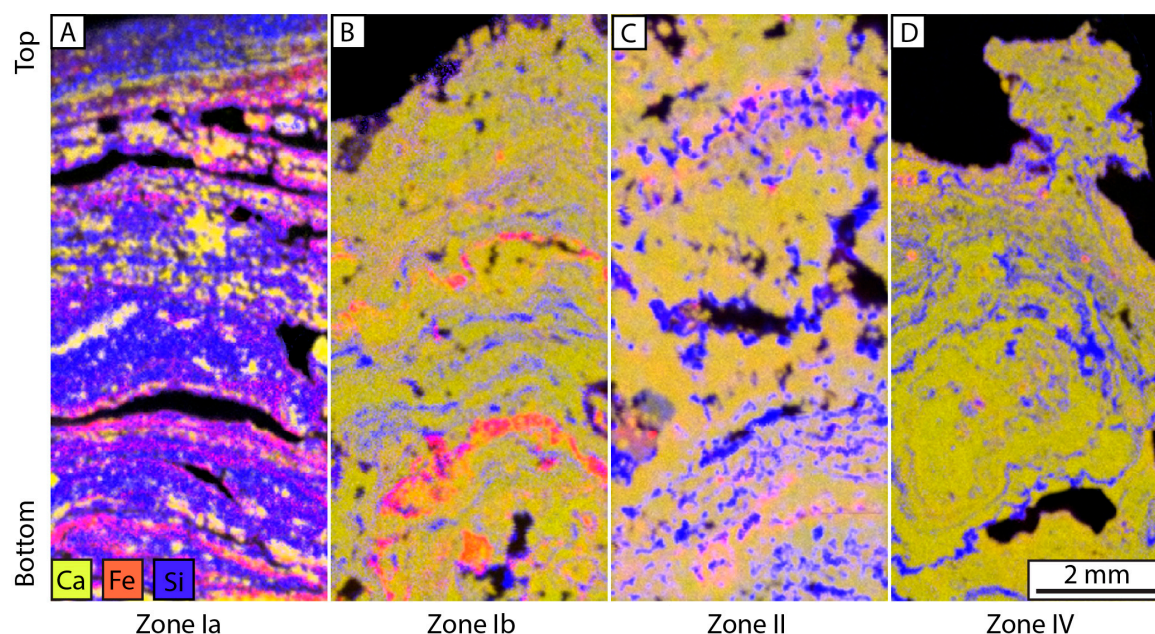


Figure 15. Micro-XRF elemental mapping (Ca in yellow, Fe in red, Si in blue, porosity in black) of the four main microbialites observed along the hydrothermal La Salsa pathway. (A) Si- and Fe-rich ledge microbialite from the central pool (Zone Ia). Most of the calcitic areas correspond to blocky calcite cements. (B) Mushroom-like microbialite from the channel (Zone Ib), showing alternations of Ca-rich, Si-rich, and rarer Fe-rich laminae. (C) Cerebroid microbialites from the apron (Zone II). Fe-rich laminae are poorly developed. (D) Cross-section of the top of a shrub microbialite from the distal zone (Zone IV). Si-rich laminae are discontinuous and Fe-rich laminae are restricted to small patches.

In the channel (Zone Ib) and apron (Zone II) aqueous silica concentration slightly decreases (72 to $67 \text{ mg}\cdot\text{L}^{-1}$), whereas the silica saturation index increases, indicating that diatoms do not compensate silica input from the source. The equal abundance of diatoms in the sediment and in the central pool suggests that residence time is lower, consistent with flowing water. Despite a decrease in temperature, which may promote silica precipitation [123,124], no significant changes in silica precipitation were observed in Zones Ia and Ib. The gap between silica saturation and effective precipitation related to temperature decrease is driven by a kinetic effect. The increasing dissolved O_2 values (Figure 7j) suggest strong photosynthetic activity, related to the green mat and diatoms. Such activity favors pH increase (from 6.3 to 7.1) by the assimilation of CO_2 and subsequent calcite oversaturation ($\text{SI}_{\text{calcite}}$ from -0.24 to $+0.61$). Consequently, CaCO_3 content and Ca/Si values increase in microbial deposits (ledges, mushroom-like structures, and cerebroids; Figure 7d,e and Figure 15A–C).

In the transitional belt (Zone III), the replacement of green mats by black mats (Figure 7c) may be explained by increases in pH and conductivity (from 52.4 to 220 mS/cm , a factor of 4.3), but also by increasing desiccation. In these distal parts, daily and annual temperature fluctuations are greater than in the proximal parts, which are constantly heated by the thermal flux. Inverted trends recorded by pH/conductivity between dry and wet conditions (high pH and lower conductivity in wet conditions and lower pH and high conductivity in dry conditions; Figure 7g,h) can be explained by (i) the absence of spillway during the dry season and (ii) the increasing influence of the climate on the hydrothermal system in the distal zone, with alternating short-lived humid and long-lasting arid periods ruling over the Pastos Grandes Laguna and, more generally, on the Altiplano [27]. Consequently, green microbial mat communities appear to require stable physicochemical conditions, with low salinity, for perennial development, which may be provided by relatively constant water inputs from the hydrothermal spring.

By contrast, black microbial mats seem to be favored by fluctuating conditions, with high salinity. The transition from green to black microbial mats may also be constrained by greater desiccation and UV radiation flux, as observed in the high-altitude Laguna Negra (Argentina, ~4000 m in elevation) [66]. This modification in microbial mat type is also visible in microbialite microfabrics, with the transition from the bundles of microbial sheaths associated with green mats to the isolated microbial sheaths associated with black mats. Bacterial composition in green and black mats was not investigated in this study, but Gomez et al. [66] noticed significant changes in bacterial families between the two types of microbial mat, which should also be the case in the Pastos Grandes Laguna.

In Zone III, the upper part of the snake-like structures shows the development of branchy structures (see Zone IV for their interpretation). Zone IV is characterized by the presence of shrubs, composed of alternating amorphous silica and calcitic laminae. These alternations locally show branchy forms, described as “ash-trays” *sensu* Risacher and Eugster [25]. Millimetric overgrowths are observed in some hydrothermal springs, indicated as spicules [12] or microstromatolites [13,19]. Shrub microfabrics and the resulting morphology are particularly controlled by the major chemical changes occurring in the distal zone. The significant decrease in aqueous silica concentration (62 to 30 mg·L⁻¹) recorded during a dry episode (January 2016) and the negative saturation index together suggest that aqueous silica has been significantly removed from the water. The presence of amorphous silica as laminae in the shrubs (Figures 12E and 13D) may argue for greater precipitation in capillary water coating emerged microbialites to the detriment of diatom accumulations, which are rare. The lower temperature observed during the wet season (~20 °C), which may fall even lower during the dry season, could explain the more abundant amorphous silica laminae [123,124]. In addition, lower pH (passing from ca. 8.5 to ca. 6.9) could be related to the sulfate reduction reaction, based on organic matter mineralization producing CO₂. The SO₄/Cl mass ratio is relatively stable from Zone I to Zone II (see Table 3) but decreases in zone IV, indicating consumption of SO₄, which can only be explained by sulfate bioreduction in the sediment (PG 1-18: Gypsum SI = -0.6; Table 3). Acidification and high conductivity values (from 48 to 225 mS·cm⁻¹) observed during a dry episode (January 2016) may explain the decrease in calcite precipitation. Conversely, the precipitation of carbonates as micritic laminae probably requires lower salinities, and higher pH, as measured during the wet season, in March 2017. Micrite may be considered here as primary microbial production [125–127]. Thin section observations suggest a transition from micrite to sparite, developing toward the edge of the shrub, but also as pendant cements under the shrub, typical of vadose precipitation [128]. These sparites mainly precipitate during the transition between wet and dry episodes, when the water level falls. The originality of La Salsa hydrothermal water chemistry, together with the extreme climatic variations in the area, may well contribute to these Ca-rich vs. Si-rich alternations. The successive precipitation of micrite, sparite, and amorphous silica indicates a high-frequency combination of abiotic and biotic processes. The term “hybrid” is particularly useful when referring to structures combining both types of processes [129]. However, the processes driving precipitation of amorphous silica and calcite are independent, as is the case for iron hydroxides, thus favoring their coexistence.

6. Conclusions

Five major hydrothermal springs emerge from the carbonate platform in the northwestern part of the Pastos Grandes Laguna. These waters, containing Ca, Si, and CO₂, generate Modern hydrothermal deposits, presented here through the detailed study of La Salsa. Two sedimentary domains are observed around this spring: a flat mound with ephemeral muddy sedimentation, and the main hydrothermal discharge with microbialite structures.

This hydrothermal discharge is divided into four principal zones along the hydrothermal pathway. Zone I forms the hydrothermal feeding system, where hot acidic waters with CO₂ bubbles emerge from a central pool, and flow through an outflow channel where numerous green microbial mats develop. Zone II corresponds to an apron on the flat mound where the flow spreads, becoming anastomosed. Zone III is defined as a proximal–distal transition belt between a poorly mineralizing environment,

and a rich mineralizing environment. Zone IV forms the distal zone of the hydrothermal system, with strong evaporative processes, and numerous mineralizing black microbial mats.

The main characteristics and interpretations of these two domains are as follows:

- (1) The flat mound is dominated by diatoms, calcitic micrite crystals, and diagenetic aragonite needles. Its origin is not yet fully elucidated, but two processes are clearly involved: (i) accumulation of mud during ephemeral flooding around the central pool and (ii) diagenetic precipitation inside the mound, enhancing its elevation by a swelling effect. Despite some morphological signs suggesting mud volcanism, sedimentary observations do not support this hypothesis.
- (2) Competition between hydrothermal influence and climatic factors plays a major role in microbialite distribution along the hydrothermal pathway, together with changes in accommodation, hydrodynamics, and substrate. Under proximal hydrothermal influence, in moderate-to-high hydrodynamic conditions, with scarce discontinuous indurated substrates, microbial deposits present ledge and mushroom-like morphologies. In lower hydrodynamic conditions, cerebroid morphologies are observed. Under climatic influence, with low hydrodynamics, snake-like and shrub morphologies dominate. Snake-like microbialites grow on cohesive sediments (with early lithification by drying-up processes) while shrubs grow on inherited carbonate platform slabs and clasts.
- (3) The Modern mixed carbonate–silicate deposition observed around the hydrothermal La Salsa spring is a good example of the complex interactions between physical, chemical, and biochemical parameters, controlling mineralogy and microfabrics distribution along a subaerial hydrological pathway. Iron hydroxides, amorphous silica, and calcite precipitate together but result from independent processes: (i) iron hydroxides from oxidation, (ii) amorphous silica during temperature cooling and/or capillary effects, and (iii) calcite when pH increases during CO₂ degassing and CO₂ assimilation through biological activity.

Many ancient thermal spring systems were devoid of diatoms, thus limiting direct comparison with La Salsa, even though similar physicochemical processes may have been in operation. Nevertheless, the Pastos Grandes Laguna is an excellent example of the complex interplay between biotic and abiotic factors in a hydrothermal spring system, with specific water chemistry, leading to a great diversity of facies and mineralogy.

Supplementary Materials: The following are available online at <http://www.mdpi.com/2075-163X/9/6/380/s1>, Table S1: Physicochemical measurements and ionic composition of an ephemeral stream and two Piedmont sources. Table S2: CaCO₃ content and Ca/Si ratio in microbialites and mud. Figure S1: Estimated mud volcano eruption depending on epicentral distance and magnitude of regional recorded earthquakes, compared to empirical liquefaction boundaries defined by Wang et al. [90] (red line) and Wang et al. [91] (interval between line of dots). Credit: U.S. Geological Survey, Earthquake Hazards Program.

Author Contributions: Conceptualization, C.B., E.V., C.D., A.V., and E.C.G.; investigation, C.B., C.D., E.M., M.M., M.C., E.G., and M.A.; writing—original draft preparation, C.B.; writing—review and editing, C.B., E.V., C.D., E.M., M.M., M.C., E.G., M.A., A.V., and E.C.G.; visualization, C.B.; supervision, A.V. and E.C.G.; project administration, A.V. and E.C.G.

Funding: This research received no external funding.

Acknowledgments: This study is a contribution from the French Total R&D (supervisor: Emmanuelle Poli), the SEDS team of the Biogéosciences Laboratory (Dijon, France), and the I-site project UB18016-BGS-IS. The authors express their gratitude to the Bolivian Total E&P, especially Olivier-Daniel Moreau, Jean-Pierre Meunier, Rozmery Cuellar, and Serge Nicoletis for technical support in Bolivia. They also thank the Sanda Andina Company for logistic contributions on site. The authors also thank the Bureau de Recherches Géologiques et Minières (BRGM) for water analyses, and Pascal Taubaty (Bourgogne Franche Comté University, Dijon), and Philippe Blanc (Lithologie Bourgogne, France) for thin section preparation. We appreciate the constructive comments from the two anonymous reviewers.

Conflicts of Interest: The authors declare no conflicts of interest.

References

1. Jones, B.; Renaut, R.W.; Rosen, M.R. Microbial biofacies in hot-spring sinters: A model based on Ohaaki Pool, North Island, New Zealand. *J. Sediment. Res.* **1998**, *68*, 413–434. [\[CrossRef\]](#)
2. Fernandez-Turiel, J.L.; Garcia-Valles, M.; Gimeno-Torrente, D.; Saavedra-Alonso, J.; Martinez-Manent, S. The hot spring and geyser sinters of El Tatio, Northern Chile. *Sediment. Geol.* **2005**, *180*, 125–147. [\[CrossRef\]](#)
3. Okumura, T.; Takashima, C.; Shiraishi, F.; Nishida, S.; Yukimura, K.; Naganuma, T.; Koike, H.; Arp, G.; Kano, A. Microbial Processes Forming Daily Lamination in an Aragonite Travertine, Nagano-yu Hot Spring, Southwest Japan. *Geomicrobiol. J.* **2011**, *28*, 135–148. [\[CrossRef\]](#)
4. Okumura, T.; Takashima, C.; Shiraishi, F.; Kano, A. Textural transition in an aragonite travertine formed under various flow conditions at Pancuran Pitu, Central Java, Indonesia. *Sediment. Geol.* **2012**, *265–266*, 195–209. [\[CrossRef\]](#)
5. Konhauser, K.O.; Phoenix, V.R.; Bottrell, S.H.; Adams, D.G.; Head, I.M. Microbial-silica interactions in Icelandic hot spring sinter: Possible analogues for some Precambrian siliceous stromatolites. *Sedimentology* **2001**, *48*, 415–433. [\[CrossRef\]](#)
6. Renaut, R.W.; Owen, R.B.; Jones, B.; Tiercelin, J.-J.; Tarits, C.; Ego, J.K.; Konhauser, K.O. Impact of lake-level changes on the formation of thermogene travertine in continental rifts: Evidence from Lake Bogoria, Kenya Rift Valley. *Sedimentology* **2013**, *60*, 428–468. [\[CrossRef\]](#)
7. Fouke, B.W.; Farmer, J.D.; Des Marais, D.J.; Pratt, L.; Sturchio, N.C.; Burns, P.C.; Discipulo, M.K. Depositional facies and aqueous-solid geochemistry of travertine-depositing hot springs (Angel Terrace, Mammoth Hot Springs, Yellowstone National Park, U.S.A.). *J. Sediment. Res.* **2000**, *70*, 565–585. [\[CrossRef\]](#)
8. Teboul, P.-A.; Durlot, C.; Gaucher, E.C.; Virgone, A.; Girard, J.-P.; Curie, J.; Lopez, B.; Camoin, G.F. Origins of elements building travertine and tufa: New perspectives provided by isotopic and geochemical tracers. *Sediment. Geol.* **2016**, *334*, 97–114. [\[CrossRef\]](#)
9. Kele, S.; Demény, A.; Siklósy, Z.; Németh, T.; Tóth, M.; Kovács, M.B. Chemical and stable isotope composition of recent hot-water travertines and associated thermal waters, from Egerszalók, Hungary: Depositional facies and non-equilibrium fractionation. *Sediment. Geol.* **2008**, *211*, 53–72. [\[CrossRef\]](#)
10. Kele, S.; Özkul, M.; Fórizs, I.; Gökgöz, A.; Baykara, M.O.; Alçiçek, M.C.; Németh, T. Stable isotope geochemical study of Pamukkale travertines: New evidences of low-temperature non-equilibrium calcite-water fractionation. *Sediment. Geol.* **2011**, *238*, 191–212. [\[CrossRef\]](#)
11. Jones, B.; Renaut, R.W.; Rosen, M.R. Biogenicity of silica precipitation around geysers and hot-spring vents, North Island, New Zealand. *J. Sediment. Res.* **1997**, *67*, 88–104. [\[CrossRef\]](#)
12. Braunstein, D.; Lowe, D.R. Relationship between spring and geyser activity and the deposition and morphology of high temperature (>73 °C) siliceous sinter, Yellowstone National Park, WY, USA. *J. Sediment. Res.* **2001**, *71*, 747–763. [\[CrossRef\]](#)
13. Renaut, R.W.; Jones, B.; Tiercelin, J.-J. Rapid in situ silicification of microbes at Loburu hot springs, Lake Bogoria, Kenya Rift Valley. *Sedimentology* **1998**, *45*, 1083–1103. [\[CrossRef\]](#)
14. White, D.E.; Brannock, W.W.; Murata, K.J. Silica in hot-spring waters. *Geochim. Cosmochim. Acta* **1956**, *10*, 27–59. [\[CrossRef\]](#)
15. Mountain, B.W.; Benning, L.G.; Boerema, J.A. Experimental studies on New Zealand hot spring sinters: Rates of growth and textural development. *Can. J. Earth Sci.* **2003**, *40*, 1643–1667. [\[CrossRef\]](#)
16. Yee, N.; Phoenix, V.R.; Konhauser, K.O.; Benning, L.G.; Ferris, F.G. The effect of cyanobacteria on silica precipitation at neutral pH: Implications for bacterial silicification in geothermal hot springs. *Chem. Geol.* **2003**, *199*, 83–90. [\[CrossRef\]](#)
17. Benning, L.G.; Phoenix, V.R.; Yee, N.; Konhauser, K.O. The dynamics of cyanobacterial silicification: An infrared micro-spectroscopic investigation. *Geochim. Cosmochim. Acta* **2004**, *68*, 743–757. [\[CrossRef\]](#)
18. Jones, B.; Renaut, R.W.; Rosen, M.R. High-temperature (>90 °C) calcite precipitation at Waikite Hot Springs, North Island, New Zealand. *J. Geol. Soc.* **1996**, *153*, 481–496. [\[CrossRef\]](#)
19. Renaut, R.W.; Jones, B.; Le Turdu, C. Calcite lily pads and ledges at Lorusio Hot Springs, Kenya Rift Valley: Travertine precipitation at the air-water interface. *Can. J. Earth Sci.* **1999**, *36*, 649–666. [\[CrossRef\]](#)
20. Campbell, K.A.; Rodgers, K.A.; Brothridge, J.M.A.; Browne, P.R.L. An unusual modern silica-carbonate sinter from Pavlova spring, Ngatamariki, New Zealand. *Sedimentology* **2002**, *49*, 835–854. [\[CrossRef\]](#)

21. Smith, D.J.; Jenkin, G.R.T.; Petterson, M.G.; Naden, J.; Fielder, S.; Toba, T.; Chenery, S.R.N. Unusual mixed silica-carbonate deposits from magmatic-hydrothermal hot springs, Savo, Solomon Islands. *J. Geol. Soc.* **2011**, *168*, 1297–1310. [\[CrossRef\]](#)
22. Guido, D.M.; Campbell, K.A. Jurassic hot Spring deposits of the Deseado Massif (Patagonia, Argentina): Characteristics and controls on regional distribution. *J. Volcanol. Geotherm. Res.* **2011**, *203*, 35–47. [\[CrossRef\]](#)
23. Wright, V.P.; Barnett, A.J. An abiotic model for the development of textures in some South Atlantic early Cretaceous lacustrine carbonates. *Geol. Soc. Lond. Spec. Publ.* **2015**, *418*, 209–219. [\[CrossRef\]](#)
24. Teboul, P.-A.; Kluska, J.-M.; Marty, N.C.M.; Debure, M.; Durllet, C.; Virgone, A.; Gaucher, E.C. Volcanic rock alterations of the Kwanza Basin, offshore Angola—Insights from an integrated petrological, geochemical and numerical approach. *Mar. Petrol. Geol.* **2017**, *80*, 394–411. [\[CrossRef\]](#)
25. Risacher, F.; Eugster, H.P. Holocene pisoliths and encrustations associated with spring-fed surface pools, Pastos Grandes, Bolivia. *Sedimentology* **1979**, *26*, 253–270. [\[CrossRef\]](#)
26. Jones, B.; Renaut, R.W. Crystal fabrics and microbiota in large pisoliths from Laguna Pastos Grandes, Bolivia. *Sedimentology* **1994**, *41*, 1171–1202. [\[CrossRef\]](#)
27. Servant-Vildary, S.; Roux, M. Multivariate analysis of diatoms and water chemistry in Bolivian saline lakes. *Hydrobiologia* **1990**, *197*, 267–290. [\[CrossRef\]](#)
28. Dupraz, C.; Reid, R.P.; Braissant, O.; Decho, A.W.; Norman, R.S.; Visscher, P.T. Processes of carbonate precipitation in modern microbial mats. *Earth Sci. Rev.* **2009**, *96*, 141–162. [\[CrossRef\]](#)
29. Muller, E.; Ader, M.; Gérard, E.; Virgone, A.; Gaucher, E.; Durllet, C.; Moreira, M.A.; Virgile, R.; Vennin, E.; Agogué, H.; et al. Carbonate Formation and Diagenesis in Pastos Grandes Laguna (Bolivia): Modern Analog for the South Atlantic Cretaceous Presalt Travertinoid Deposits. In Proceedings of the AGU Fall Meeting, New Orleans, LA, USA, 11–15 December 2017.
30. Bougeault, C.; Durllet, C.; Vennin, E.; Muller, E.; Mercuzot, M.; Gérard, E.; Ader, M.; Virgone, A.; Gaucher, E.C. Atypical carbonate-silica mineralisations under biotic and abiotic controls: The Modern hydrothermal example of Pastos Grandes Laguna (Bolivia). In Proceedings of the 20th International Sedimentological Congress, Québec City, QC, Canada, 13–17 August 2018.
31. Allmendinger, R.W.; Jordan, T.E.; Kay, S.M.; Isacks, B.L. The evolution of the Altiplano-Puna Plateau of the Central Andes. *Annu. Rev. Earth Planet. Sci.* **1997**, *25*, 139–174. [\[CrossRef\]](#)
32. Isacks, B.L. Uplift of the Central Andean Plateau and Bending of the Bolivian Orocline. *J. Geophys. Res.* **1988**, *93*, 3211–3231. [\[CrossRef\]](#)
33. Tibaldi, A.; Corazzato, C.; Rovida, A. Miocene–Quaternary structural evolution of the Uyuni–Atacama region, Andes of Chile and Bolivia. *Tectonophysics* **2009**, *471*, 114–135. [\[CrossRef\]](#)
34. de Silva, S.L. Altiplano–Puna volcanic complex of the central Andes. *Geology* **1989**, *17*, 1102–1106. [\[CrossRef\]](#)
35. de Silva, S.; Zandt, G.; Trumbull, R.; Viramonte, J.G.; Salas, G.; Jiménez, N. Large ignimbrite eruptions and volcano-tectonic depressions in the Central Andes: A thermomechanical perspective. *Geol. Soc. Lond. Spec. Publ.* **2006**, *269*, 47–63. [\[CrossRef\]](#)
36. Salisbury, M.J.; Jicha, B.R.; de Silva, S.L.; Singer, B.S.; Jiménez, N.C.; Ort, M.H. $^{40}\text{Ar}/^{39}\text{Ar}$ chronostratigraphy of Altiplano–Puna volcanic complex ignimbrites reveals the development of a major magmatic province. *Geol. Soc. Am. Bull.* **2011**, *123*, 821–840. [\[CrossRef\]](#)
37. Chmielowski, J.; Zandt, G.; Haberland, C. The Central Andean Altiplano-Puna Magmatic Body. *Geophys. Res. Lett.* **1999**, *26*, 783–786. [\[CrossRef\]](#)
38. Ward, K.M.; Zandt, G.; Beck, S.L.; Christensen, D.H.; McFarlin, H. Seismic imaging of the magmatic underpinnings beneath the Altiplano-Puna volcanic complex from the joint inversion of the surface wave dispersion and receiver functions. *Earth Planet. Sci. Lett.* **2014**, *404*, 43–53. [\[CrossRef\]](#)
39. Kaiser, J.F. Understanding Large Resurgent Calderas and Associated Magma Systems: The Pastos Grandes Caldera Complex, Southwest Bolivia. Ph.D. Thesis, Oregon State University, Corvallis, OR, USA, 2014.
40. Kaiser, J.F.; de Silva, S.; Schmitt, A.K.; Economos, R.; Sunagua, M. Million-year melt-presence in monotonous intermediate magma for a volcanic-plutonic assemblage in the Central Andes: Contrasting histories of crystal-rich and crystal-poor super-sized silicic magmas. *Earth Planet. Sci. Lett.* **2017**, *457*, 73–86. [\[CrossRef\]](#)
41. Peel, M.C.; Finlayson, B.L.; McMahon, T.A. Updated world map of the Köppen-Geiger climate classification. *Hydrol. Earth Syst. Sci.* **2007**, *4*, 439–473. [\[CrossRef\]](#)
42. Risacher, F. Le cadre géochimique des bassins à évaporites des Andes boliviennes. *Cah. ORSTOM Sér. Géol.* **1978**, *10*, 37–48.

43. Iltis, A.; Risacher, F.; Servant-Vildary, S. Contribution à l'étude hydrobiologique des lacs salés du sud de l'Altiplano bolivien. *Rev. Hydrobiol. Trop.* **1984**, *17*, 259–273.
44. Risacher, F.; Fritz, B. Geochemistry of Bolivian salars, Lipez, southern Altiplano: Origin of solutes and brine evolution. *Geochim. Cosmochim. Acta* **1991**, *55*, 687–705. [[CrossRef](#)]
45. Ballivian, O.; Risacher, F. *Los Salares del Altiplano Boliviano: Métodos de Estudio y Estimación Económica*; ORSTOM: Paris, France, 1981; 246p.
46. Ahlfeld, F. Sodaseen in Lipez (Bolivien). *Neues Jb. Miner. Mh.* **1956**, *6*, 128–136.
47. Badaut, D.; Risacher, F. Authigenic smectite on diatom frustules in Bolivian saline lakes. *Geochim. Cosmochim. Acta* **1983**, *47*, 363–375. [[CrossRef](#)]
48. Abdelouas, A. Etude de l'altération de Verres Rhyolitiques au Contact de Saumures Naturelles (Bolivie)—Application à L'étude du Comportement à Long Terme du Verre Nucléaire R7T7. Ph.D. Thesis, Université Louis Pasteur, Strasbourg, France, 1996.
49. Alonso, R.N.; Viramonte, J.G. Borate deposits in the Andes. In *Stratabound Ore Deposits in the Andes*; Fontboté, L., Amstutz, G.C., Cardozo, E., Frutos, J., Eds.; Springer: Berlin, Germany, 1990; pp. 721–732.
50. Kasemann, S.A.; Meixner, A.; Erzinger, J.; Viramonte, J.G.; Alonso, R.N.; Franz, G. Boron isotope composition of geothermal fluids and borate minerals from salar deposits (central Andes/NW Argentina). *J. S. Am. Earth Sci.* **2004**, *16*, 685–697. [[CrossRef](#)]
51. Rouchy, J.M.; Servant, M.; Fournier, M.; Causse, C. Extensive carbonate algal bioherms in upper Pleistocene saline lakes of the central Altiplano of Bolivia. *Sedimentology* **1996**, *43*, 973–993. [[CrossRef](#)]
52. Sylvestre, F.; Servant, M.; Servant-Vildary, S.; Causse, C.; Fournier, M.; Ybert, J.-P. Lake-Level Chronology on the Southern Bolivian Altiplano (18–23°) during Late-Glacial Time and the Early Holocene. *Quat. Res.* **1999**, *51*, 54–66. [[CrossRef](#)]
53. Blard, P.-H.; Sylvestre, F.; Tripathi, A.K.; Claude, C.; Causse, C.; Coudrain, A.; Condom, T.; Seidel, J.-L.; Vimeux, F.; Moreau, C.; et al. Lake highstands on the Altiplano (Tropical Andes) contemporaneous with Heinrich 1 and the Younger Dryas: New insights from ^{14}C , U–Th dating and $\delta^{18}\text{O}$ of carbonates. *Quat. Sci. Rev.* **2011**, *30*, 3973–3989. [[CrossRef](#)]
54. Placzek, C.J.; Quade, J.; Patchett, P.J. A 130 ka reconstruction of rainfall on the Bolivian Altiplano. *Earth Planet. Sci. Lett.* **2013**, *363*, 97–108. [[CrossRef](#)]
55. Fontes, J.C.; Servant, M. *Dataciones Radiométricas Sobre el Cuaternario Reciente del Altiplano de Bolivia*; Primer Congreso Geológico de Bolivia-Potosí: Potosí, Bolivia, 1976.
56. Shapiro, R.S. A Comment on the Systematic Confusion of Thrombolites. *Palaios* **2000**, *15*, 166–169. [[CrossRef](#)]
57. Burne, R.V.; Moore, L.S. Microbialites: Organosedimentary deposits of benthic microbial communities. *Palaios* **1987**, *2*, 241–254. [[CrossRef](#)]
58. Parkhurst, D.L.; Appelo, C.A.J. *Description of Input and Examples for PHREEQC Version 3: A Computer Program for Speciation, Batch Reaction, one Dimensional Transport, and Inverse Geochemical Calculations*; 6-A43; U.S. Geological Survey Techniques and Methods: Reston, VA, USA, 2013; 497p.
59. Blanc, P.; Lassin, A.; Piantone, P.; Azaroual, M.; Jacquemet, N.; Fabbri, A.; Gaucher, E.C. Thermoddem: A geochemical database focused on low temperature water/rock interactions and waste materials. *Appl. Geochem.* **2012**, *27*, 2107–2116. [[CrossRef](#)]
60. Mazzullo, S.J.; Birdwell, B.A. Syngenetic formation of grainstones and pisolites from fenestral carbonates in peritidal settings. *J. Sediment. Res.* **1989**, *59*, 605–611. [[CrossRef](#)]
61. Wright, V.P. Paleosols in shallow marine carbonate sequences. *Earth Sci. Rev.* **1994**, *35*, 367–395. [[CrossRef](#)]
62. Flügel, E. *Microfacies of Carbonate Rocks: Analysis, Interpretation and Application*; Springer: Berlin, Germany, 2004; 976p.
63. Eugster, H.P.; Jones, B.F. Behavior of major solutes during closed-basin brine evolution. *Am. J. Sci.* **1979**, *279*, 609–631. [[CrossRef](#)]
64. Pace, A.; Bourillot, R.; Bouton, A.; Vennin, E.; Galaup, S.; Bundeleva, I.; Patrier, P.; Dupraz, C.; Thomazo, C.; Sansjofre, P.; et al. Microbial and diagenetic steps leading to the mineralisation of Great Salt Lake microbialites. *Sci. Rep.* **2016**, *6*, 31495. [[CrossRef](#)] [[PubMed](#)]
65. Pace, A.; Bourillot, R.; Bouton, A.; Vennin, E.; Braissant, O.; Dupraz, C.; Duteil, T.; Bundeleva, I.; Patrier, P.; Galaup, S.; et al. Formation of stromatolite lamina at the interface of oxygenic-anoxygenic photosynthesis. *Geobiology* **2018**, *16*, 378–398. [[CrossRef](#)] [[PubMed](#)]

66. Gomez, F.J.; Mlewski, C.; Boidi, F.J.; Farías, M.E.; Gérard, E. Calcium Carbonate Precipitation in Diatom-rich Microbial Mats: The Laguna Negra Hypersaline Lake, Catamarca, Argentina. *J. Sediment. Res.* **2018**, *88*, 727–742. [[CrossRef](#)]
67. Mlewski, E.C.; Pisapia, C.; Gomez, F.; Lecourt, L.; Rueda, E.S.; Benzerara, K.; Ménez, B.; Borensztajn, S.; Jamme, F.; Réfrégiers, M.; et al. Characterization of Pustular Mats and Related Rivularia-Rich Laminations in Oncoids From the Laguna Negra Lake (Argentina). *Front. Microbiol.* **2018**, *9*, 996. [[CrossRef](#)]
68. Servant-Vildary, S. Les diatomées des sédiments superficiels de quelques lacs salés de Bolivie. *Bull. Sci. Géol.* **1983**, *36*, 249–253. [[CrossRef](#)]
69. Chafetz, H.S.; Folk, R.L. Travertines: Depositional morphology and the bacterially constructed constituents. *J. Sediment. Res.* **1984**, *54*, 289–316. [[CrossRef](#)]
70. Guidry, S.A.; Chafetz, H.S. Anatomy of siliceous hot springs: Examples from Yellowstone National Park, Wyoming, USA. *Sediment. Geol.* **2003**, *157*, 71–106. [[CrossRef](#)]
71. Jones, B.; Renaut, R.W. Impact of seasonal changes on the formation and accumulation of soft siliceous sediments on the discharge apron of Geysir, Iceland. *J. Sediment. Res.* **2010**, *80*, 17–35. [[CrossRef](#)]
72. Pentecost, A. *Travertine*; Springer: Berlin, Germany, 2005; 445p.
73. French, H.M. *The Periglacial Environment*, 3rd ed.; John Wiley & Sons Ltd.: Chichester, UK, 2007; 458p.
74. Trombotto, D.T. Survey of cryogenic processes, periglacial forms and permafrost conditions in South America. *Rev. Inst. Geol.* **2000**, *21*, 33–55. [[CrossRef](#)]
75. Francou, B.; Le Méhauté, N.; Jomelli, V. Factors Controlling Spacing Distances of Sorted Stripes in a Low-Latitude, Alpine Environment (Cordillera Real, 16 °S, Bolivia). *Permafr. Periglac.* **2001**, *12*, 367–377. [[CrossRef](#)]
76. Kessler, M.A.; Werner, B.T. Self-Organization of Sorted Patterned Ground. *Science* **2003**, *299*, 380–383. [[CrossRef](#)] [[PubMed](#)]
77. Husen, S.; Taylor, R.; Smith, R.B.; Healsen, H. Changes in geyser eruption behavior and remotely triggered seismicity in Yellowstone National Park produced by the 2002 M7.9 Denali fault earthquake, Alaska. *Geology* **2004**, *32*, 537–540. [[CrossRef](#)]
78. Wang, C.-Y.; Manga, M. *Earthquakes and Water*; Springer: Berlin, Germany, 2009; 249p.
79. Wotton, R.S. The ubiquity and many roles of exopolymers (EPS) in aquatic systems. *Sci. Mar.* **2004**, *68*, 13–21. [[CrossRef](#)]
80. Gratier, J.P.; Frery, E.; Deschamps, P.; Røyne, A.; Renard, F.; Dysthe, D.; Ellouz-Zimmerman, N.; Hamelin, B. How travertine veins grow from top to bottom and lift the rocks above them: The effect of crystallization force. *Geology* **2012**, *40*, 1015–1018. [[CrossRef](#)]
81. Frery, E.; Gratier, J.P.; Ellouz-Zimmerman, N.; Deschamps, P.; Blamart, D.; Hamelin, B.; Swennen, R. Geochemical transect through a travertine mount: A detailed record of CO₂-enriched fluid leakage from Late Pleistocene to present-day—Little Grand Wash fault (Utah, USA). *Quat. Int.* **2017**, *437*, 98–106. [[CrossRef](#)]
82. Mazzini, A.; Svensen, H.; Hovland, M.; Plancke, S. Comparison and implications from strikingly different authigenic carbonates in a Nyegga complex pockmark, G11, Norwegian Sea. *Mar. Geol.* **2006**, *231*, 89–102. [[CrossRef](#)]
83. Mazzini, A.; Ivanov, M.K.; Nermoen, A.; Bahr, A.; Bohrmann, G.; Svensen, H.; Plancke, S. Complex plumbing systems in the near subsurface: Geometries of authigenic carbonates from Dolgovskoy Mound (Black Sea) constrained by analogue experiments. *Mar. Petrol. Geol.* **2008**, *25*, 457–472. [[CrossRef](#)]
84. Vanneste, H.; Kastner, M.; James, R.H.; Connelly, D.P.; Fisher, R.E.; Kelly-Gerreyn, B.A.; Heeschen, K.; Haackel, M.; Mills, R.A. Authigenic carbonates from the Darwin Mud Volcano, Gulf of Cadiz: A record of palaeo-seepage of hydrocarbon bearing fluids. *Chem. Geol.* **2012**, *300–301*, 24–39. [[CrossRef](#)]
85. Hedberg, H. Relation of Methane Generation to Undercompacted Shales, Shale Diapirs, and Mud Volcanoes. *AAPG Bull.* **1974**, *58*, 661–673.
86. Mazzini, A.; Etiope, G. Mud volcanism: An updated review. *Earth-Sci. Rev.* **2017**, *168*, 81–112. [[CrossRef](#)]
87. Svensen, H.; Karlsen, D.A.; Sturz, A.; Backer-Owe, K.; Banks, D.A.; Plancke, S. Processes controlling water and hydrocarbon composition in seeps from the Salton Sea geothermal system, California, USA. *Geology* **2007**, *35*, 85–88. [[CrossRef](#)]
88. Onderdonk, N.; Mazzini, A.; Shafer, L.; Svensen, H. Controls on the geomorphic expression and evolution of gryphons, pools, and caldera features at hydrothermal seeps in the Salton Sea Geothermal Field, southern California. *Geomorphology* **2011**, *130*, 327–342. [[CrossRef](#)]

89. Galli, P. New empirical relationships between magnitude and distance for liquefaction. *Tectonophysics* **2000**, *324*, 169–187. [[CrossRef](#)]
90. Wang, C.-Y.; Manga, M.; Wong, A. Floods on Mars released from groundwater by impact. *Icarus* **2005**, *175*, 551–555. [[CrossRef](#)]
91. Wang, C.-Y.; Wong, A.; Dreger, D.S.; Manga, M. Liquefaction Limit during Earthquakes and Underground Explosions: Implications on Ground-Motion Attenuation. *Bull. Seismol. Soc. Am.* **2006**, *96*, 355–363. [[CrossRef](#)]
92. Bonini, M. Mud volcano eruptions and earthquakes in the Northern Apennines and Sicily, Italy. *Tectonophysics* **2009**, *474*, 723–735. [[CrossRef](#)]
93. Rudolph, M.L.; Manga, M. Mud volcano response to the 4 April 2010 El Mayor-Cucapah earthquake. *J. Geophys. Res.* **2010**, *115*, B12211. [[CrossRef](#)]
94. Herdianita, N.R.; Browne, P.R.L.; Rodgers, K.A.; Campbell, K.A. Mineralogical and textural changes accompanying of silica sinter. *Miner. Deposita* **2000**, *35*, 48–62. [[CrossRef](#)]
95. Jones, B.; Renaut, R.W. Microstructural changes accompanying the opal-A to opal-CT transition: New evidence from the siliceous sinters of Geysir, Haukadalur, Iceland. *Sedimentology* **2007**, *54*, 921–948. [[CrossRef](#)]
96. Williams, L.A.; Parks, G.A.; Crerar, D.A. Silica Diagenesis, I. Solubility controls. *J. Sediment. Res.* **1985**, *55*, 301–311. [[CrossRef](#)]
97. Lewin, J.C. The dissolution of silica from diatom walls. *Geochim. Cosmochim. Acta* **1961**, *21*, 182–198. [[CrossRef](#)]
98. Ryves, D.B.; Battarbee, R.W.; Juggins, S.; Fritz, S.C.; Anderson, N.J. Physical and chemical predictors of diatom dissolution in freshwater and saline lake sediments in North America and West Greenland. *Limnol. Oceanogr.* **2006**, *51*, 1355–1368. [[CrossRef](#)]
99. Dupraz, C.; Fowler, A.; Tobias, C.; Visscher, P.T. Stromatolitic knobs in Storr’s Lake (San Salvador, Bahamas): A model system for formation and alteration of laminae. *Geobiology* **2013**, *11*, 527–548. [[CrossRef](#)]
100. Jahnert, R.J.; Collins, L.B. Controls on microbial activity and tidal flat evolution in Shark Bay, Western Australia. *Sedimentology* **2013**, *60*, 1071–1099. [[CrossRef](#)]
101. Bouton, A.; Vennin, E.; Pace, A.; Bourillot, R.; Dupraz, C.; Thomazo, C.; Brayard, A.; Désaubliaux, G.; Visscher, P.T. External controls on the distribution, fabrics and mineralization of modern microbial mats in a coastal hypersaline lagoon, Cayo Coco (Cuba). *Sedimentology* **2016**, *63*, 972–1016. [[CrossRef](#)]
102. Roche, A.; Vennin, E.; Bouton, A.; Olivier, N.; Wattinne, A.; Bundeleva, I.; Deconinck, J.-F.; Virgone, A.; Gaucher, E.C.; Visscher, P.T. Oligo-Miocene lacustrine microbial and metazoan buildups from the Limagne Basin (French Massif Central). *Palaeogeogr. Palaeoclimatol. Palaeoecol.* **2018**, *504*, 34–59. [[CrossRef](#)]
103. Warden, J.G.; Coshell, L.; Rosen, M.R.; Breecker, D.O.; Ruthrof, K.X.; Omelon, C.R. The importance of groundwater flow to the formation of modern thrombolytic microbialites. *Geobiology* **2019**. [[CrossRef](#)] [[PubMed](#)]
104. Andres, M.S.; Reid, R.P. Growth morphologies of modern marine stromatolites: A case study from Highborne Cay, Bahamas. *Sediment. Geol.* **2006**, *185*, 319–328. [[CrossRef](#)]
105. Casanova, J. Les Stromatolites Continentaux: Paléoécologie, Paléohydrologie, Paléoclimatologie. Application au Rift Gregory. Ph.D. Thesis, University Aix-Marseille II, Marseille, France, 1986.
106. Casanova, J.; Hillaire-Marcel, C. Late Holocene hydrological history of Lake Tanganyika, East Africa, from isotopic data on fossil stromatolites. *Palaeogeogr. Palaeoclimatol. Palaeoecol.* **1992**, *91*, 35–48. [[CrossRef](#)]
107. Ginsburg, R.N.; Planavsky, N.J. Diversity of Bahamian Microbialite Substrates. In *Links Between Geological Processes, Microbial Activities & Evolution of Life*; Dylek, Y., Furnes, H., Muehlenbachs, K., Eds.; Springer: Berlin, Germany, 2008; pp. 177–195.
108. Bouton, A.; Vennin, E.; Boule, J.; Pace, A.; Bourillot, R.; Thomazo, C.; Brayard, A.; Désaubliaux, G.; Goslar, T.; Yokoyama, Y.; et al. Linking the distribution of microbial deposits from the Great Salt Lake (Utah, USA) to tectonic and climatic processes. *Biogeosciences* **2016**, *13*, 5511–5526. [[CrossRef](#)]
109. Manzo, E.; Perri, E.; Tucker, M.E. Carbonate deposition in a fluvial tufa system: Processes and products (Corvino Valley–Southern Italy). *Sedimentology* **2012**, *59*, 553–577. [[CrossRef](#)]
110. Pedley, M.; Rogerson, M.; Middleton, R. Freshwater calcite precipitates from *in vitro* mesocosm flume experiments: A case for biomediation of tufas. *Sedimentology* **2009**, *56*, 511–527. [[CrossRef](#)]

111. Roche, A.; Vennin, E.; Bundeleva, I.; Payandi-Rolland, D.; Bouton, A.; Gaucher, E.C.; Amiotte-Suchet, P.; Courvoisier, H.; Visscher, P.T. The role of substrate on the mineralization potential of microbial mats in a modern freshwater river (Villiers-le-Bâcle, France). *Minerals* **2019**, *9*, 359. [\[CrossRef\]](#)
112. Dill, R.F. Subtidal stromatolites, ooids and crusted-lime muds at the Great Bahama Bank Margin. In *From Shoreline to Abyss*; Osborn, R.F., Ed.; SEPM: Tulsa, OK, USA, 1991; Volume 46, pp. 147–171.
113. Basso, D.; Bracchi, V.A.; Favalli, A.N. Microbialite formation in southern Sinai (Egypt). *Facies* **2013**, *59*, 7–18. [\[CrossRef\]](#)
114. Leggitt, V.L.; Cushman, R.A., Jr. Complex caddisfly-dominated bioherms from the Eocene Green River Formation. *Sediment. Geol.* **2001**, *145*, 377–396. [\[CrossRef\]](#)
115. Della Porta, G. Carbonate build-ups in lacustrine, hydrothermal and fluvial settings: Comparing depositional geometry, fabric types and geochemical signature. *Geol. Soc. Lond. Spec. Publ.* **2015**, *418*, 17–68. [\[CrossRef\]](#)
116. Stockner, J.G. Observations of Thermophilic Algal Communities in Mount Rainier and Yellowstone National Parks. *Limnol. Oceanogr.* **1967**, *12*, 13–17. [\[CrossRef\]](#)
117. Owen, R.B.; Renaut, R.W.; Hover, V.C.; Ashley, G.M.; Muasya, A.M. Swamps, springs and diatoms: Wetlands of the semi-arid Bogoria-Baringo Rift, Kenya. *Hydrobiologia* **2004**, *518*, 59–78. [\[CrossRef\]](#)
118. Owen, R.B.; Renaut, R.W.; Jones, B. Geothermal diatoms: A comparative study of floras in hot spring systems of Iceland, New Zealand, and Kenya. *Hydrobiologia* **2008**, *610*, 175–192. [\[CrossRef\]](#)
119. Winsborough, B.M.; Golubić, S. The role of diatoms in stromatolite growth: Two examples from modern freshwater settings. *J. Phycol.* **1987**, *23*, 195–201. [\[CrossRef\]](#)
120. Gomez, F.J.; Kah, L.C.; Bartley, J.K.; Astini, R.A. Microbialites in a high-altitude Andean lake: Multiple controls on carbonate precipitation and lamina accretion. *Palaios* **2014**, *29*, 233–249. [\[CrossRef\]](#)
121. Arp, G.; Wedemeyer, N.; Reitner, J. Fluvial Tufa Formation in a Hard-Water Creek (Deinschwanger Bach, Franconian Alb, Germany). *Facies* **2001**, *44*, 1–22. [\[CrossRef\]](#)
122. Phoenix, V.R.; Konhauser, K.O.; Ferris, F.G. Experimental study of iron and silica immobilization by bacteria in mixed Fe-Si systems: Implications for microbial silicification in hot springs. *Can. J. Earth. Sci.* **2003**, *40*, 1669–1678. [\[CrossRef\]](#)
123. Walther, J.V.; Helgeson, H.C. Calculation of the thermodynamic properties of aqueous silica and the solubility of quartz and its polymorphs at high pressures and temperatures. *Am. J. Sci.* **1977**, *277*, 1315–1351. [\[CrossRef\]](#)
124. Williams, L.A.; Crerar, D.A. Silica diagenesis, II. General mechanisms. *J. Sediment. Res.* **1985**, *55*, 312–321. [\[CrossRef\]](#)
125. Visscher, P.T.; Reid, R.P.; Bebout, B.M.; Hoefft, S.E.; Macintyre, I.G.; Thompson, J.A., Jr. Formation of lithified micritic laminae in modern marine stromatolites (Bahamas): The role of sulfur cycling. *Am. Mineral.* **1998**, *83*, 1482–1493. [\[CrossRef\]](#)
126. Visscher, P.T.; Reid, R.P.; Bebout, B.M. Microscale observations of sulfate reduction: Correlation of microbial activity with lithified micritic laminae in modern marine stromatolites. *Geology* **2000**, *28*, 919–922. [\[CrossRef\]](#)
127. Dupraz, C.; Visscher, P.T.; Baumgartner, L.K.; Reid, R.P. Microbe-mineral interactions: Early carbonate precipitation in a hypersaline lake (Eleuthera Island, Bahamas). *Sedimentology* **2004**, *51*, 745–765. [\[CrossRef\]](#)
128. Freytet, P.; Verrecchia, E. Les carbonates continentaux du pourtour méditerranéen: Microfaciès et milieux de formation. *Méditerranée* **1989**, *68*, 5–28. [\[CrossRef\]](#)
129. Riding, R. Abiogenic, microbial and hybrid authigenic carbonate crusts: Components of Precambrian stromatolites. *Geol. Croat.* **2008**, *61*, 73–103.

